Neutrinos from type Ia supernovae: The gravitationally confined detonation scenario

Warren P. Wright, James P. Kneller, Sebastian T. Ohlmann, Friedrich K. Röpke, Kate Scholberg, and Ivo R. Seitenzahl

Neutrinos from Type Ia Supernovae: The Gravitationally Confined Detonation Scenario

Warren P. Wright,[1, *] James P. Kneller,[1, †] Sebastian T. Ohlmann,[2, ‡]

Friedrich K. Röpke,[2, 3, §] Kate Scholberg,[4, ¶] and Ivo R. Seitenzahl[5, 6, **]

[1]*Department of Physics, North Carolina State University, Raleigh, North Carolina 27695, USA*

[2]*Heidelberger Institut für Theoretische Studien,*

Schloss-Wolfsbrunnenweg 35, D-69118 Heidelberg, Germany

[3]*Zentrum für Astronomie der Universität Heidelberg,*

Institut für Theoretische Astrophysik, Philosophenweg 12, D-69120 Heidelberg, Germany

[4]*Department of Physics, Duke University, Durham NC 27708, USA*

[5]*Research School of Astronomy and Astrophysics,*

Australian National University, Canberra, ACT 2611, Australia

[6]*ARC Centre of Excellence for All-Sky Astrophysics (CAASTRO)*

Despite their use as cosmological distance indicators and their importance in the chemical evolution of Galaxies, the unequivocal identification of the progenitor systems and explosion mechanism of normal Type Ia supernovae (SNe Ia) remains elusive. The leading hypothesis is that such a supernova is a thermonuclear explosion of a carbon-oxygen white dwarf but the exact explosion mechanism is still a matter of debate. Observation of a Galactic SN Ia would be of immense value in answering the many open questions related to these events. One potentially useful source of information about the explosion mechanism and progenitor is the neutrino signal because the neutrinos from the different mechanisms possess distinct spectra as a function of time and energy.

In this paper we compute the expected neutrino signal from a Gravitationally Confined Detonation (GCD) explosion scenario for a SN Ia and show how the flux at Earth contains features in time and energy unique to this scenario. We then calculate the expected event rates in the Super-K, Hyper-K, JUNO, DUNE, and IceCube detectors and find both Hyper-K and IceCube will see a few events for a GCD supernova at 1 kpc or closer, while Super-K, JUNO, and DUNE will see events if the supernova is closer than $\sim$0.3 kpc. The distance and detector criteria needed to resolve the time and spectral features arising from the explosion mechanism, neutrino production, and neutrino oscillation processes are also discussed.

The neutrino signal from the GCD is then compared with the signal from a Deflagration-to-Detonation Transition (DDT) explosion model computed previously. We find the overall event rate is the most discriminating feature between the two scenarios followed by the event rate time structure. Using the event rate in the Hyper-K detector alone, the DDT can be distinguished from the GCD at 2σ if the distance to the supernova is less than 2.3 kpc for a

normal mass ordering and 3.6 kpc for an inverted ordering.

I. INTRODUCTION

The stellar explosions known as Thermonuclear - or Type Ia - supernovae are important phenomena in astrophysics. SNe Ia are the distance indicators [1, 2] which indicate the Universe is accelerating [3–5] and SNe Ia are also major contributors to the chemical evolution of Galaxies [6, 7] leading to notable changes in the rate at which, for example, oxygen and iron are enriched when the contribution from SNe Ia becomes significant. But despite their importance, little is known about the progenitors of these supernovae. Only in a few cases for nearby SNe Ia, such as SN 2011fe or SN 2014J, do pre-explosion images place strong constraints upon the luminosity of the progenitor system [8–10]. Nevertheless, various arguments point towards a paradigm that SNe Ia are the explosion of a carbon-oxygen White Dwarf in a binary system that accretes sufficient mass from its companion to begin explosive carbon burning. The source of the accreted mass may be another, smaller, white dwarf (a double degenerate scenario) or a main sequence or giant star (a single degenerate scenario). The reader is referred to Maoz, Mannucci & Nelemans [11] and Ruiz-Lapuente [12] for reviews and variations upon these scenarios.

In addition to the debate over the identity of the companion, another debate is over the mechanism for the explosion itself. Popular mechanisms for the single degenerate scenario at the present time are the delayed detonation transition model (DDT) model [13], the gravitationally confined detonation (GCD) model [14], and the pulsational reverse detonation (PRD) model [15], though others also exist. We refer the reader to Hillebrandt *et al.* [16] for a recent review. Determining the explosion mechanism from observation will be difficult. The unknown identity of the progenitor means observatories will require close to full sky coverage, while the brevity of the explosion - simulations indicate the star becomes unbound within a few seconds - means sub-second integration times. Thus it may not be until there is a Galactic SN Ia that the explosion mechanism can be determined observationally. The rate of SNe Ia in the Galaxy is calculated to be $1.4^{+1.4}_{-0.8}$ per century by Adams *et al.* [17] and represents $\sim 30\%$ of the total supernova rate. Adams *et al.* calculate the most probable distance to a Galactic SN Ia to be $d = 9$ kpc.

* wpwright@ncsu.edu
† jpknelle@ncsu.edu
‡ sebastian.ohlmann@h-its.org
§ friedrich.roepke@h-its.org
¶ schol@phy.duke.edu
** ivo.seitenzahl@anu.edu.au

At such close proximity, when the next SN Ia occurs within the Galaxy not only can we exploit electromagnetic observations, it may also be possible to obtain information about the progenitor and explosion mechanism in the gravitational waves and the neutrino signal. The gravitational wave emission of the explosion (not the inspiral) has been considered by Falta *et al.* [18] and Seitenzahl *et al.* [19]. The neutrino emission was calculated by Kunugise & Iwamoto [20], Odrzywolek & Plewa [21], and Seitenzahl *et al.* [19]. The study by Odrzywolek & Plewa [21] is particularly worth emphasizing because they showed how the neutrinos are capable of distinguishing between explosion mechanisms even when the electromagnetic output is identical.

But as with many things neutrino related, detecting the neutrino signal from SNe Ia is not easy. In comparison with core-collapse supernovae, the flux of neutrinos at Earth from a SN Ia is approximately four orders of magnitude smaller for a source at the same distance and also the spectrum peaks in the range of 3 MeV [20] rather than the $10 - 20$ MeV for the neutrino spectrum from a core-collapse SN. The shift to lower energies reduces the number of events one expects in a detector because of the energy dependence of neutrino cross sections and, furthermore, detecting the events is harder because they occur much closer to, or below, detector thresholds. However one advantage of the neutrinos from SNe Ia compared to core-collapse SNe is that the neutrino signal is more reliably calculated. The densities in the core of SNe Ia are not sufficient to trap the neutrinos so there is no neutrino transport to follow and there are also no neutrino self-interaction effects [22, 23] because the neutrino density is not large enough.

The advent of several next-generation neutrino detectors recently prompted Wright *et al.* [24] (hereafter called Paper I) to recompute the expected signal from a DDT SN Ia explosion including many effects which had not been taken into account previously. For their calculation, Wright *et al.* took into account the full time and energy dependence of the emission and calculated the neutrino flavor transformation as a function of time and energy through the supernova and along several rays through the simulation in order to study the line-of-sight variability. They then processed the fluxes at Earth using the SNOwGLoBES detector event rate calculation software so as to compute the total and differential event rates in the Super-K, Hyper-K, JUNO, and DUNE detectors. A separate analysis was undertaken for the signal in the IceCube detector. Their conclusion was that despite the difficulties, neutrino detectors are becoming so large and sensitive that the neutrinos from a DDT SN Ia at the Galactic center can be detected. As the supernova is placed closer to Earth, features in the spectrum as a function of time and energy may be observed.

The goal of this paper is to repeat the calculations of Paper I, but this time for the neutrino signal from the alternative scenario of a Gravitationally Confined Detonation. The strategy is very

similar to that found in Paper I and the outline of our paper is as follows. In Sec. II we provide an outline of the Gravitationally Confined Detonation simulation we adopt. We then describe in Sec. III the method by which the simulation is post-processed to compute the emitted neutrino spectra followed by Sec. IV, where we calculate the neutrino flavor transformation through the simulation as a function of time and energy along different rays. In Sec. V we combine the emitted spectra and neutrino flavor transition probabilities to compute the flux at Earth and send these fluxes through the SNOwGLoBES software for representative examples of various neutrino detector technologies. The total and differential event rates we compute are investigated in order to determine how well the GCD supernova can be observed in neutrinos for a range of of distances to the event. Finally we compare the GCD and DDT neutrino signals in Sec. VI in order to determine the distance/detector requirements necessary to distinguish the two scenarios. We conclude with Sec. VII.

II.   SUPERNOVA SIMULATION

The SN explosion model used in our calculations is a gravitationally confined detonation (GCD) model. The explosion starts with off-center deflagration ignition in a near-Chandrasekhar-mass white dwarf (WD). This ignition is of a single bubble near the star's center and deflagration ash quickly 'floats' to the surface creating a 'plume'. The ash is prevented from escaping by the star's gravity. The gravitationally confined ash then proceeds to engulf the surface of the star converging upon a location opposite to the initial eruption point of the plume on the surface. The convergence of the ash leads to a compression which plausibly ignites a detonation [25] that quickly propagates through the star unbinding it completely. This type of explosion mechanism was first discussed in [26] and the particular implementation of this scenario model used in our paper is taken from Seitenzahl *et al.* [27] where the full details can be found. In what follows we provide a brief review. The explosion is modeled in 3D by use of the hydrodynamic SN code LEAFS on a 512^3 grid. This same code was also used to simulate a deflagration-to-detonation transition (DDT) model in [28] used in Paper I. The deflagration and detonation flames are modeled using a levelset approach (29, for more details see also 27). For reference, we summarize the basic properties of the two models in Table I.

The most significant difference between the two simulations is that for the GCD case the detonation is handled differently because the DDT module is turned off: the detonation is initiated here after 2.37 s, when the deflagration ashes converge at one point and compress the material to high enough densities and temperatures. The detonation is then initiated by placing an ignition kernel

Model	IGE [$M_\odot$]	^{56}Ni [$M_\odot$]	IME [$M_\odot$]	E_{kin} [10^{51} erg]
GCD	0.844	0.742	0.415	1.38
N100	0.839	0.604	0.454	1.45

TABLE I. Compilation of the asymptotic kinetic energy (E_{kin}) and nucleosynthesis yields for the Iron group elements (IGE), ^{56}Ni, and intermediate mass elements (IME) in solar masses ($M_\odot$) for the GCD [27] and N100 [28] explosion models.

at this spot using a second levelset function to track the detonation front. The similarities between the two simulations make comparing the neutrino signals from each largely dependent on the explosion mechanism (DDT or GCD) and not as dependent on the other simulation details. This is useful considering the high computational cost of these calculations. For the reader's reference, the GCD simulation we use is the case where the initial stellar central density is 2.9×10^9 g cm^{-3} with a temperature of 5×10^5 K and the composition is taken to be carbon and oxygen with an initial $Y_e = 0.49886$.

The progression of the SN is depicted in Fig. 1. This figure consists of 14 subplots, each of which contain a title detailing the time since deflagration and the scale of the subplot (length of the blue 'axes'). Each subplot also has a legend describing the density contours shown in the two stellar density contour-plots to the left of the legend. In each subplot, the left contour-plot has the white deflagration contour set to opaque to view the exterior development and the right contour-plot has the white deflagration contour set to semi-transparent to allow visualization of the interior evolution. From 2.5 s onward, the detonation contour is plotted in green. In all subplots, the 10 blue radial lines represent the ten neutrino trajectories that we examine in order to determine the line-of-sight dependence. One of these trajectories aligns with the initial plume of deflagration burning while another aligns with the point of detonation on the surface. Fig. 1 clearly shows how the initial deflagration ash rises to the surface, spreads around the star, collides opposite to the initial emergence point, and how a detonation is initiated there, which spreads quickly throughout the star. Initially only neutrinos which propagate along the plume are affected by the unfolding explosion. The effects of the explosion quickly move to five of the ten trajectories, then nine of ten, and finally all the trajectories we consider are affected. Once the detonation begins, the sequence of affected rays repeats but in the opposite order: the ray last affected during the deflagration phase is the first to be affected by the detonation. The effects of the detonation then spread to the five rays last affected by detonation, then nine rays out of the ten, and finally all ten. Thus we learn the GCD is a highly asymmetrical explosion and while the neutrinos may be emitted more-or-less isotropically because the matter is not sufficiently dense to trap them, we might expect significant
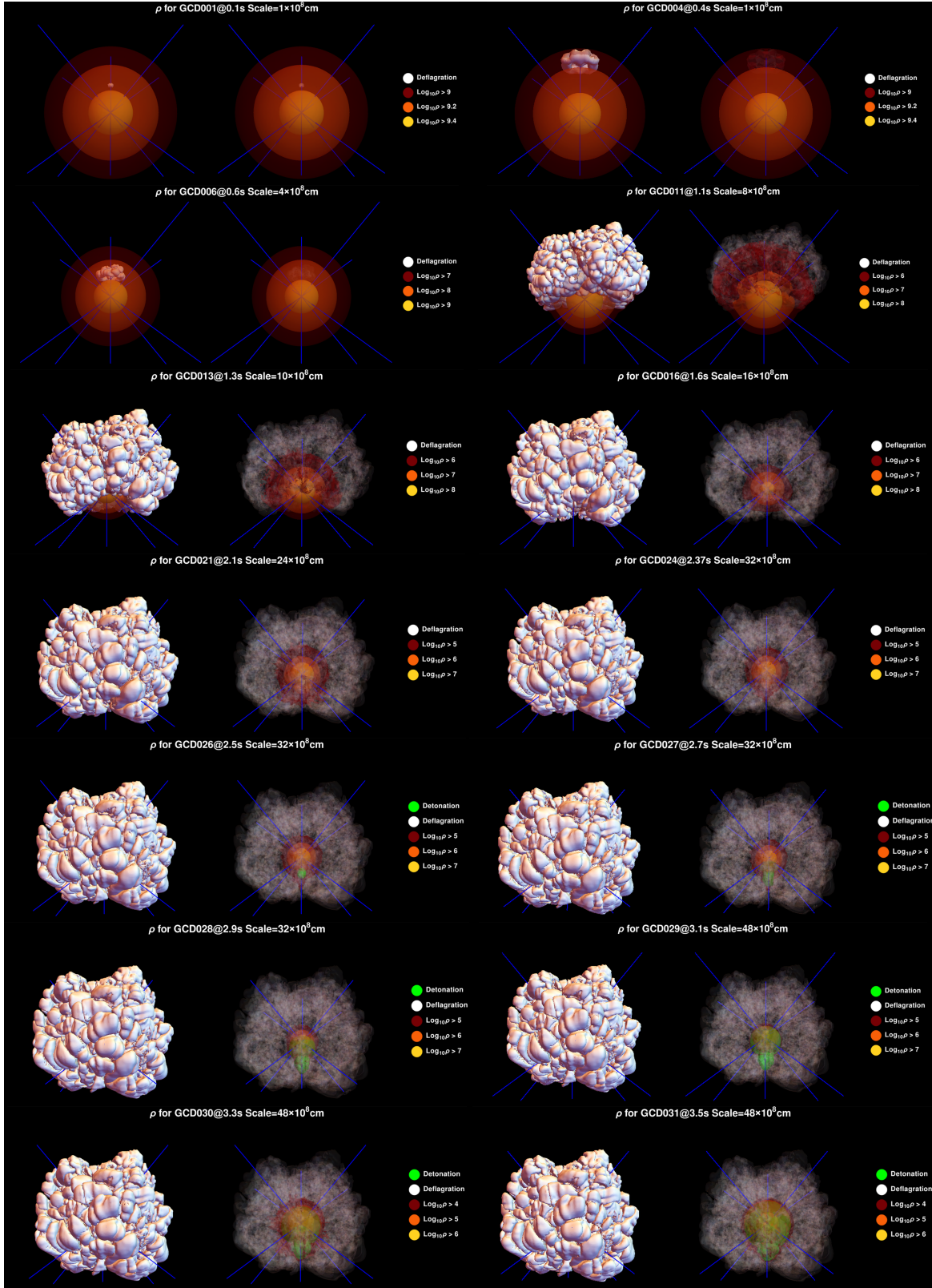
FIG. 1. Density contour plots including deflagration (white) and detonation (green) surfaces.

viewing-angle dependence on the neutrino signal due to the density profile dependence of neutrino flavor transformation. The detectability of this dependence is explored in Sec. V.

Finally, we should point out there is an important difference between the material burnt under deflagration conditions compared to that burnt during the detonation. The deflagration naturally produces turbulence whereas the detonation does not. One of the effects of turbulence is to create a complicated structure for the location of the deflagration flame fronts hence a highly structured profile of density discontinuities. Furthermore the location of the turbulent material in the GCD scenario is quite different from that in the DDT scenario. In the GCD the detonation region is entirely interior to the mostly exterior deflagration region; in the DDT the deflagration region was closer to the center of the star and much of the detonation region was exterior. We shall see the compound density discontinuities in the deflagration ash on the exterior of the GCD supernova will leave an imprint in the neutrinos, but first we consider the luminosity and neutrino spectra emitted from the explosion.

III. NEUTRINO PRODUCTION

The neutrino production of the GCD simulation is calculated using the same 'NSE only' strategy as in Paper I and used by Odrzywolek & Plewa [21]. This strategy means we only include the zones in Nuclear Statistical Equilibrium (NSE) where $T > 3 \times 10^9$ K. As shown in Paper I, these zones account for the bulk of the emission of neutrinos. The emissivity of these zones is calculated using the software package NuLib [30–37]. The weak processes included in our calculation are electron and positron capture on free protons, neutrons, and nuclei. The only thermal process included is electron-positron pair annihilation, which is the dominant emission process for the stellar conditions under examination.

Figure 2 shows the neutrino luminosity as a function of time for the GCD simulation. The blue (black) lines and dots represent the $\nu_e(\bar{\nu}_e)$ luminosity arising due to weak processes and the red lines and dots represent the luminosity in all six flavors arising due to pair production. We observe from the figure that the neutrino emission from a GCD scenario occurs in two bursts both lasting about 1 s with a gap of around 1.5 s between them. The reason for the lack of neutrino emission between ~ 1.3 s and ~ 2.5 s - which corresponds to the period when the deflagration spreads over the surface of the star - is because we find the simulation does not contain any zones hot enough to be in NSE during this period. The double burst of neutrinos is a characteristic feature of the GCD explosion mechanism. The neutrinos are produced under very different conditions during the
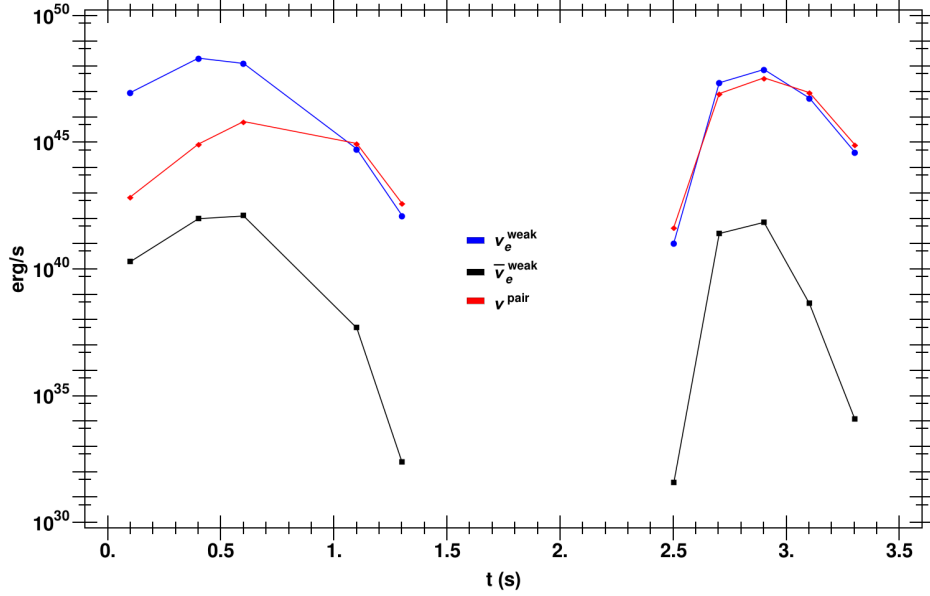
FIG. 2. GCD total neutrino luminosity for electron neutrino and electron anti neutrino weak processes, and for pair production (all flavors). The dots represent the actual calculation and the lines are a linear interpolation. The middle gap in neutrino emission results from a lack of any NSE stellar zones for these times.

two bursts. During the first burst the material is burning under deflagration conditions and so we shall refer to it as the deflagration neutrino burst; during the second the neutrinos are produced by matter burning under detonation conditions so we shall refer to this second burst as the detonation burst. Despite the different burning conditions, the figure indicates the overall neutrino luminosity during the two bursts are very similar. Closer inspection does reveal a difference: the figure indicates the contribution from thermal processes only begins to be important towards the end of the deflagration burst whereas it is important for the entirety of the detonation burst. Finally, the figure indicates the $\bar{\nu}_e$ luminosity arising due to weak processes is vastly superseded by the $\bar{\nu}_e$ luminosity arising due to thermal processes. Electron antineutrino emission from weak processes occurs as a consequence of positron capture by neutrons in nuclei and, at these temperatures and densities, these reactions are energetically disfavored.

Our results are similar to the findings of Odrzywolek & Plewa for their Y12 GCD model, with a few differences. The total energy radiated by neutrinos in our model is about a factor of six lower compared to their result, mostly due to the fact that their model burns more mass during the deflagration. Since most of the neutrino luminosity is due to electron captures on free protons during the deflagration phase, the amount of mass burned in the deflagration is the most important factor in determining the total energy carried by neutrinos. The main reason why the Y12 model

burns more mass in the deflagration is that the simulations are performed in 2D with assumed azimuthal rotational symmetry, unlike the GCD200 model, which is a full 3D simulation. With this imposed symmetry, deflagration bubbles in 2D away from the z-axis effectively turn into tori, which enlarges the volume burned compared to a 3D simulation.

We also observe the detonation burst occurs about $\sim$1 s earlier in our simulation than in the Y12 model of Odrzywolek & Plewa. We attribute this difference largely to the different assumed ignition conditions, in particular the initial offset of the deflagration spark. The deflagration of the Y12 model evolves and rises much more slowly compared to the GCD200 model. The Rayleigh-Taylor (RT) growth rate scales as the square root of the local acceleration due to gravity. Our GCD200 deflagration is ignited at an offset distance of 200 km from the center, whereas the Y12 ignition occurs a mere 12.5 km offset from the center. The closer the ignition to the center, the smaller the gravity and the slower the growth-rate of the RT-instability and hence the slower the evolution of the deflagration. The fact that their model uses a lower central density $2.0 \times 10^9 \, \mathrm{g \, cm^{-3}}$ vs $2.9 \times 10^9 \, \mathrm{g \, cm^{-3}}$) further amplifies the difference. We have chosen a 200 km offset because our 3D simulations have shown that smaller offsets do not lead to detonations [27].

The spectral features associated with the GCD SN are presented in Fig. 3. The top six plots represent the luminosity for the 6 neutrino flavors for the five time slices corresponding to the initial deflagration burning phase. The bottom six plots represent the luminosity for the six neutrino flavors for the five time slices corresponding to the final detonation burning. Fig. 3 indicates that initially the ν_e luminosity is much larger than the luminosity in other flavors but by midway through the deflagration burst the luminosity in all flavors is similar and remains this way for the later detonation burst. We also observe in the figure a spectral feature at ~ 10 MeV (mostly from electron capture on copper [24]) which is absent initially in the deflagration burst but then emerges at $t \sim 1$ s and remains present in the spectrum for the entirety of the detonation burst.

IV. NEUTRINO FLAVOR TRANSFORMATION

The neutrino flavor composition of the spectra emitted in the supernova are not what will be detected at Earth due to the flavor transformations as the neutrinos propagate through the supernova and due to decoherence on the journey to Earth. This has the potential to mix the time and spectral features of one flavor with those of another. The flavor transformations are dependent on the density and electron fraction of the material through which the neutrinos must propagate
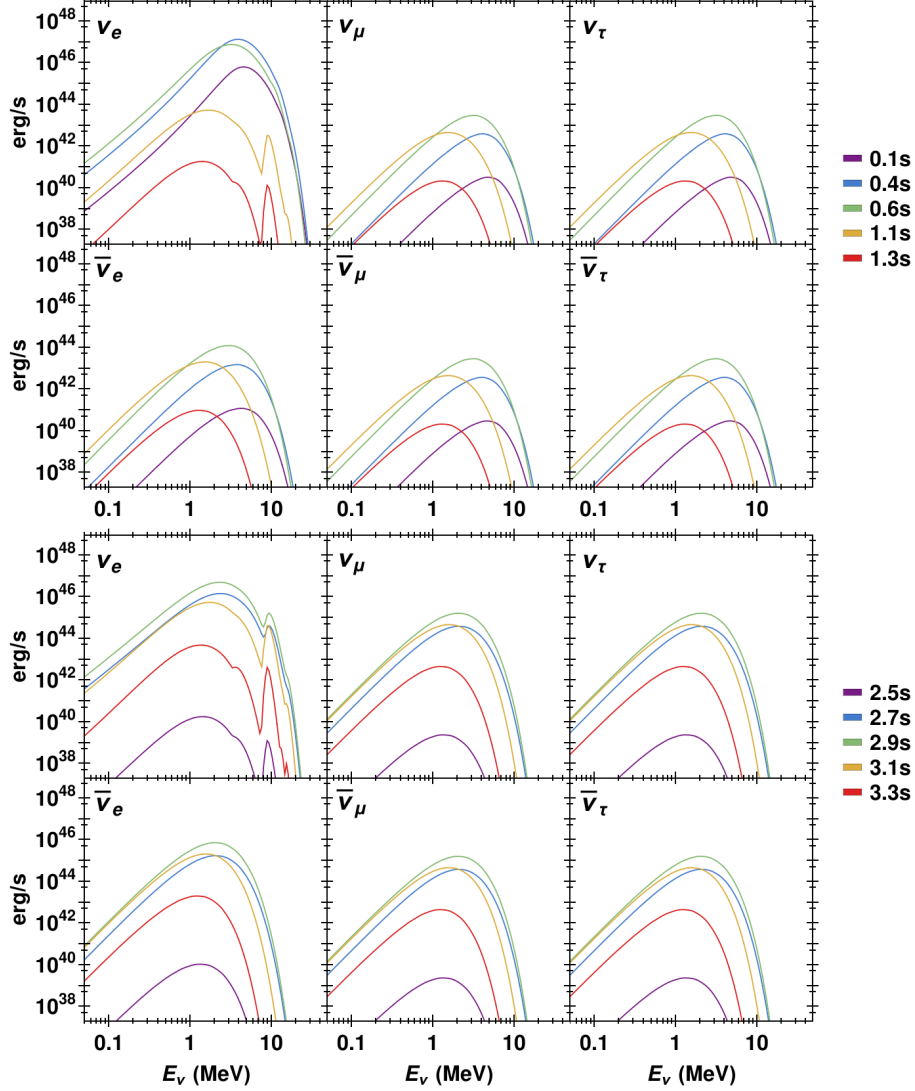
FIG. 3. GCD neutrino luminosity spectra. Each curve is the sum of all considered weak and thermal processes. The top plots represent the initial (0.1 s < t < 1.3 s) neutrino burst corresponding to the initial deflagration and the bottom plots represent the secondary (2.5 s < t < 3.3 s) neutrino burst corresponding to the detonation.

[38, 39]. The density profiles along two lines of sight through the simulation are shown in Fig. 4: the density profiles along the deflagration plume (left panel) and its polar opposite along the ray that passes through the detonation point (right panel). This density plot can reveal the effects of turbulence as departures from the smooth density profile seen at $t = 0.1$ s. The turbulent effects in the high density deflagration ash during the early deflagration phase are shown in the leftmost panel for $2 \times 10^8 < r$ (cm) $< 5 \times 10^8$. While the turbulent effects in the low density deflagration ash during the later detonation phase are shown in the rightmost panel for $4 \times 10^8 < r$ (cm) $< 2 \times 10^9$.
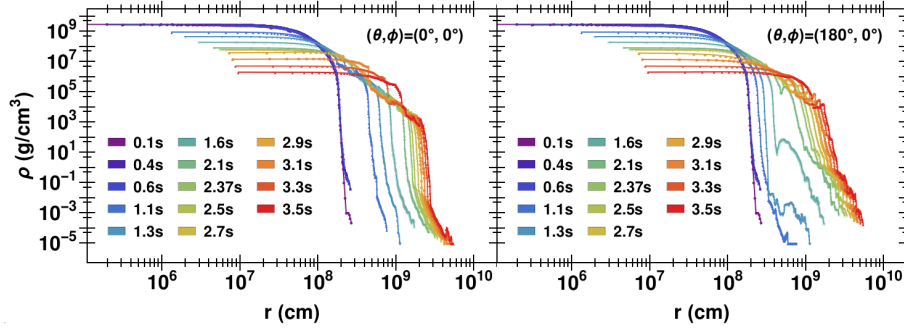
FIG. 4. Density profiles for various time slices of the GCD simulation. The left panel represents the trajectory that is aligned with the initial deflagration plume (positive z-axis) . The right panel represents the trajectory opposite to the left panel's trajectory, i.e. the trajectory aligned with where detonation is initiated (negative z-axis).

Along both rays, the non-trivial density profiles mean we cannot assume adiabatic neutrino flavor propagation. Instead, the flavor transition probabilities are computed numerically following the same protocol as Paper I. Since the calculation and many of the features in the results are the same as in Paper I, in what follows we just present the results of the transformation calculations.

A. Matter basis transformation probabilities

The neutrino transformation calculations are undertaken and presented in the matter basis in order to remove the trivial mixing in the flavor basis. As a reference, in dense matter and the normal mass ordering (NMO) the electron neutrino flavor is closely aligned with the matter basis state ν_3 and the electron antineutrino with matter basis state $\bar{\nu}_1$. For an inverted mass ordering (IMO) the electron flavor in dense matter is closely aligned with the matter basis state ν_2 and the electron antineutrino with matter basis state $\bar{\nu}_3$. In vacuum, the electron flavor neutrino is approximately 70% matter state ν_1 and 30% matter state ν_2, the electron antineutrino is $\sim 70\%$ matter state $\bar{\nu}_1$ and 30% matter state $\bar{\nu}_2$.

The matter basis transition probabilities $P_{ij}^{(\mathrm{m})} = P(\nu_j^{(\mathrm{m})} \to \nu_i^{(\mathrm{m})})$ for a neutrino that was initially state j in the matter basis to be detected as state i in the matter basis after the neutrinos have propagated through the SN depend upon the the neutrino mass orderings, the line of sight and the epoch. We have computed the transition probabilities at the ten different snapshot times indicated by the points in Fig. 3 but here show just the results at the two points of maximum luminosity, namely, at the peak of the deflagration neutrino burst at $t = 0.4$ s and at the peak of the detonation neutrino burst at $t = 2.9$ s.
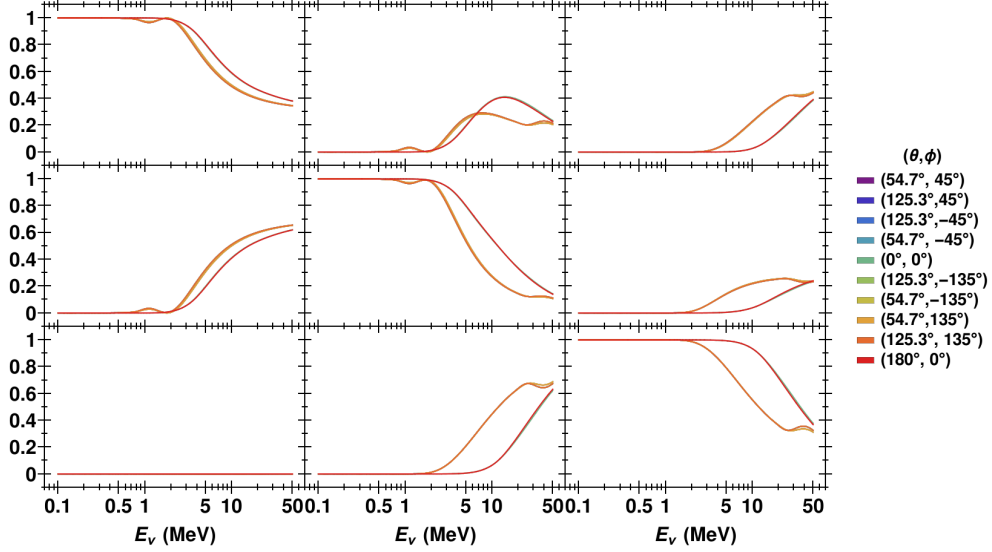
FIG. 5. The neutrino matter basis transition probabilities $P_{ij}^{(\mathrm{m})}(E_\nu)$ as a function of energy. The top row, from left to right, shows $P_{11}^{(\mathrm{m})}$, $P_{12}^{(\mathrm{m})}$ and $P_{13}^{(\mathrm{m})}$. The middle row from left to right shows $P_{21}^{(\mathrm{m})}$, $P_{22}^{(\mathrm{m})}$ and $P_{23}^{(\mathrm{m})}$ and the bottom row from left to right shows $P_{31}^{(\mathrm{m})}$, $P_{32}^{(\mathrm{m})}$ and $P_{33}^{(\mathrm{m})}$. The mass ordering is normal and the snapshot time is $t = 0.4$ s. The polar and azimuth angles of each trajectory are given in the legend.
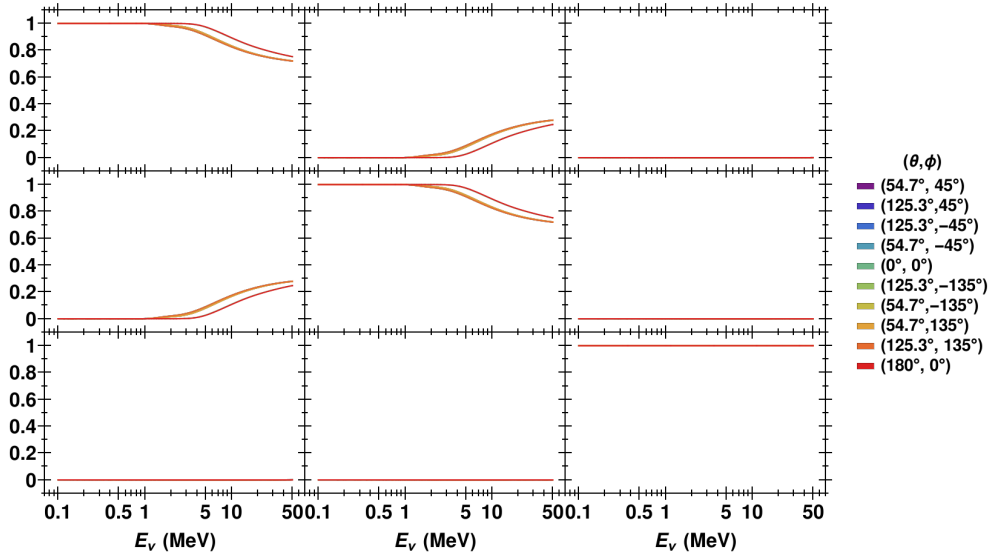
FIG. 6. The antineutrino matter basis transition probabilities for normal mass ordering at $t = 0.4$ **s**. The structure and layout is the same as that of Fig. 5.

At the deflagration peak ($t = 0.4$ s), Fig. 5 shows that for $E_\nu \lesssim 1$ MeV, the neutrino transition probabilities in the NMO are adiabatic ($P_{ij} \sim \delta_{ij}$) for all ten lines of sight considered. However, for $E_\nu > 1$ MeV, the neutrino transition probabilities in the NMO become partially diabatic. The diabaticity is a consequence of the very steep density profile at the edge of the star at this epoch.
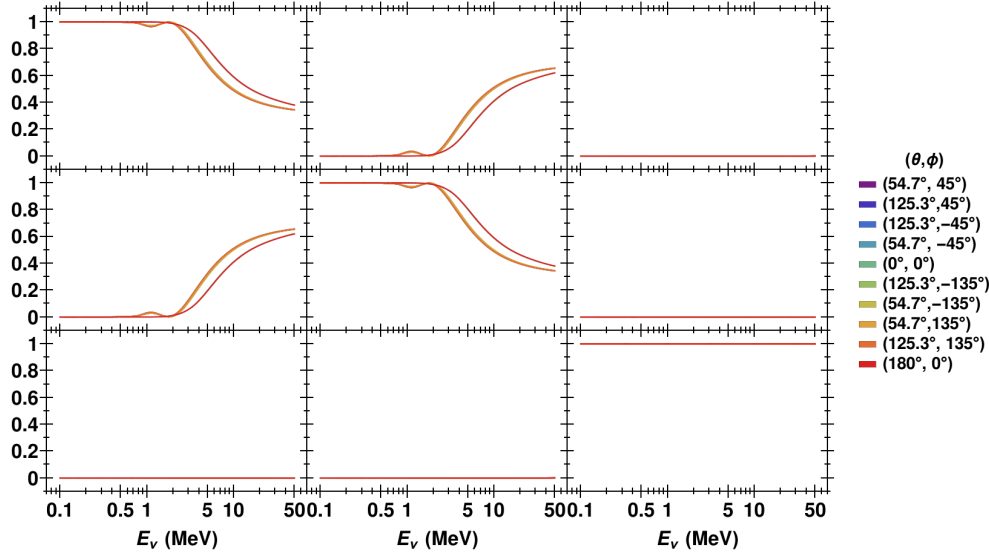
FIG. 7. The neutrino matter basis transition probabilities for inverted mass ordering at $t = 0.4$ **s**. The structure and layout is the same as that of Fig. 5.

The transition probabilities also exhibit line-of-sight dependence since the transition probability versus energy curves in the figure depend upon the exact trajectory the neutrinos take through the star. The line-of-sight dependence at this epoch is almost binary and the curves fall into two groups depending upon whether or not the neutrinos have to traverse the deflagration plume. The effect is substantial with a line-of-sight variation as big as 50% difference for $E \sim 10$ MeV in the $P_{33}^{(\mathrm{m})}$ channel. This change in $P_{33}^{(\mathrm{m})}$ can have consequences for the signal, because for a NMO, the electron flavor neutrinos are closely aligned with matter state ν_3 in dense matter whereas matter state ν_3 in the vacuum has very little electron flavor content.

At the same epoch Fig. 6 shows the transition probabilities for the antineutrinos again in the NMO. For this mass ordering the propagation is adiabatic except in the $\bar{\nu}_1 \leftrightarrow \bar{\nu}_2$ channel where we find some mixing occurs for energies above $E_\nu \gtrsim 1$ MeV which depends upon the line of sight. For this mass ordering and at this epoch, the amount of mixing and the line of sight variability in the antineutrinos is not as large as the mixing in the same channel for the neutrinos.

That situation changes if we swap the neutrino mass ordering. For the IMO the neutrino and antineutrino transition probabilities at the peak of the deflagration burst are shown in Figs. 7 and Fig. 8. Now the mixing channels involving ν_3 are totally adiabatic with zero line of sight dependence. The mixing between ν_1 and ν_2 is very similar to the NMO with adiabatic propagation up to $E_\nu \sim 5$ MeV and partially adiabatic thereafter. The line of sight dependence in the IMO is only a difference in the transition probabilities of $\sim 10\%$ at most. For the antineutrinos and
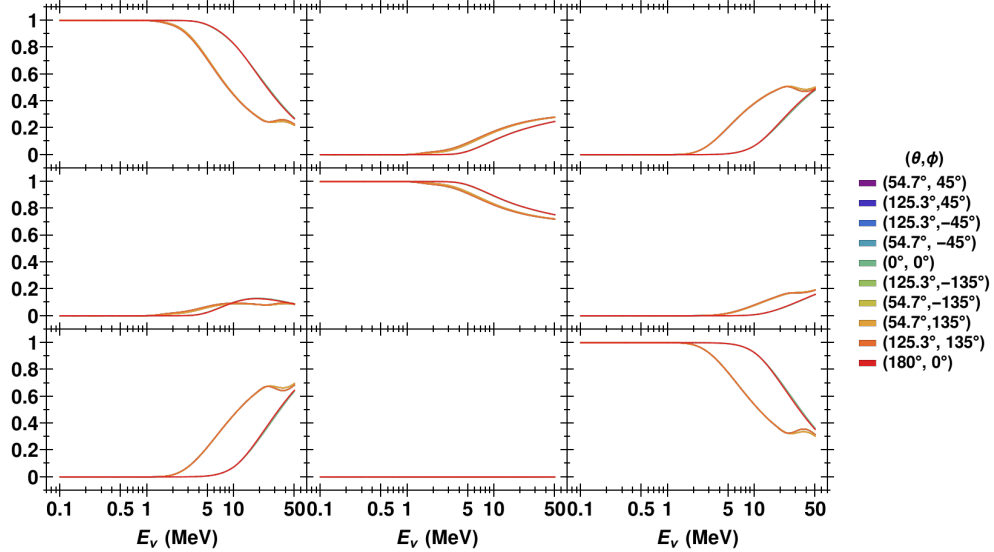
FIG. 8. The antineutrino matter basis transition probabilities for inverted mass ordering at $t = 0.4$ **s**. The structure and layout is the same as that of Fig. 5.

the IMO we also observe adiabaticity in all channels up to $E_\nu \sim 5$ MeV with partial adiabatic evolution for high energies. As seen previously in other mixing scenarios, at this epoch the transition probabilities as a function of energy can be grouped into one of two groups depending upon whether the deflagration plume was crossed. As for the NMO, the fact that the matter basis probabilities are not adiabatic has consequences for the signal we expect. For an IMO the electron flavor in dense matter aligns with matter state ν_2: in vacuum matter state ν_2 is only 30% electron flavor. Conversion of matter state ν_2 to ν_1 which is 70% electron flavor in vacuum boosts the observability of the original electron neutrino spectrum by more than double.

The line of sight dependence at $t = 0.4$ s is essentially binary. If we consider the later epoch of $t = 2.9$ s at the peak of the detonation burst the line of sight dependence becomes much more extreme. The transition probabilities in the NMO for the neutrinos and antineutrinos at the detonation burst peak are shown in Figs. 9 and 10 respectively. When compared to Figs. 5 and 6 we see each line of sight produces a unique curve. The difference from one to the next can be as large as 100% for the neutrinos and $E \gtrsim 5$ MeV. The lower energy neutrinos and antineutrinos no longer evolve adiabatically in any channel except $P_{31}^{(m)}$. At higher energies, $E \gtrsim 5$ MeV, the variability in $P_{22}^{(m)}$, $P_{23}^{(m)}$, $P_{32}^{(m)}$ and $P_{33}^{(m)}$ appears to be much larger than at $t = 0.4$ s but, in contrast, the transition probabilities $P_{11}^{(m)}$, $P_{12}^{(m)}$, $P_{13}^{(m)}$ and $P_{21}^{(m)}$ at higher energies are closer to adiabatic than at the previous epoch. The same is also true for the higher energies antineutrinos in this mass ordering at this epoch: the variability between the different lines of sight has increased
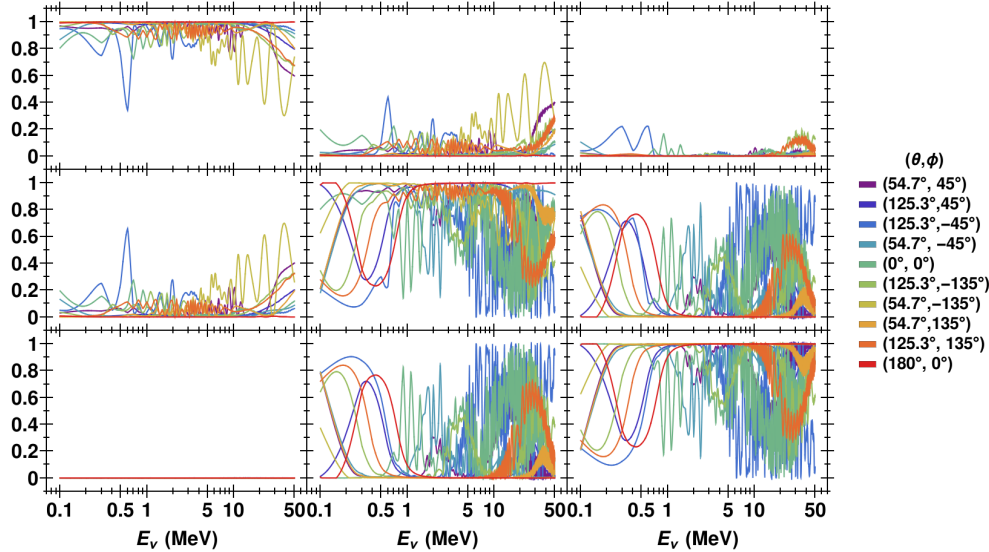
FIG. 9. The neutrino matter basis transition probabilities for normal mass ordering at $t = 2.9$ s. The structure and layout is the same as that of Fig. 5.
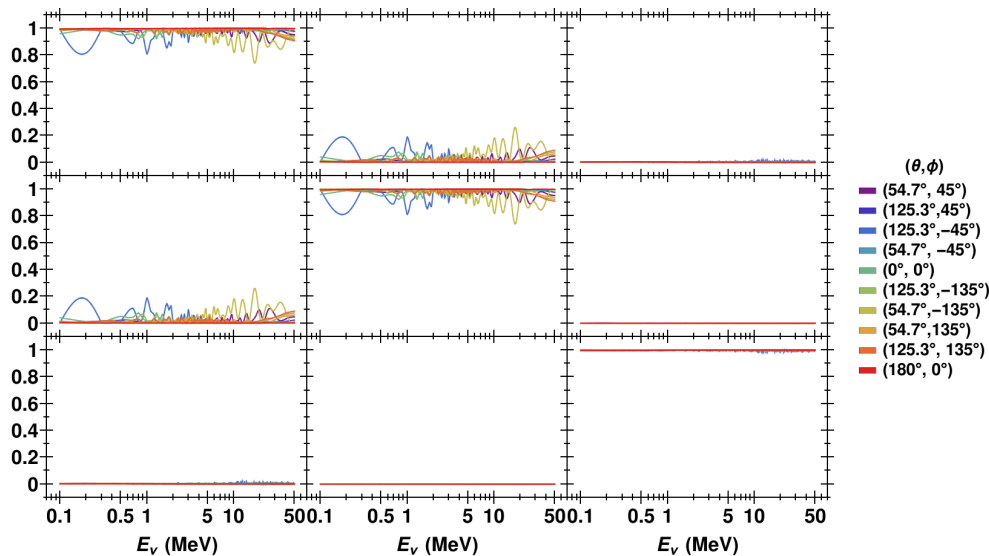

FIG. 10. The antineutrino matter basis transition probabilities for normal mass ordering at $t = 2.9$ s. The structure and layout is the same as that of Fig. 5.

but the overall trend is towards greater adiabaticity for $E \gtrsim 5$ MeV. This evolution is similar to what was seen in Paper I for the DDT case where it was explained as due to a softening of the density gradients as the star explodes. Figure 4 indicates there is a similar softening for the GCD scenario.

Finally, Figs. 11 and 12 show the transition probabilities at the detonation peak when we switch
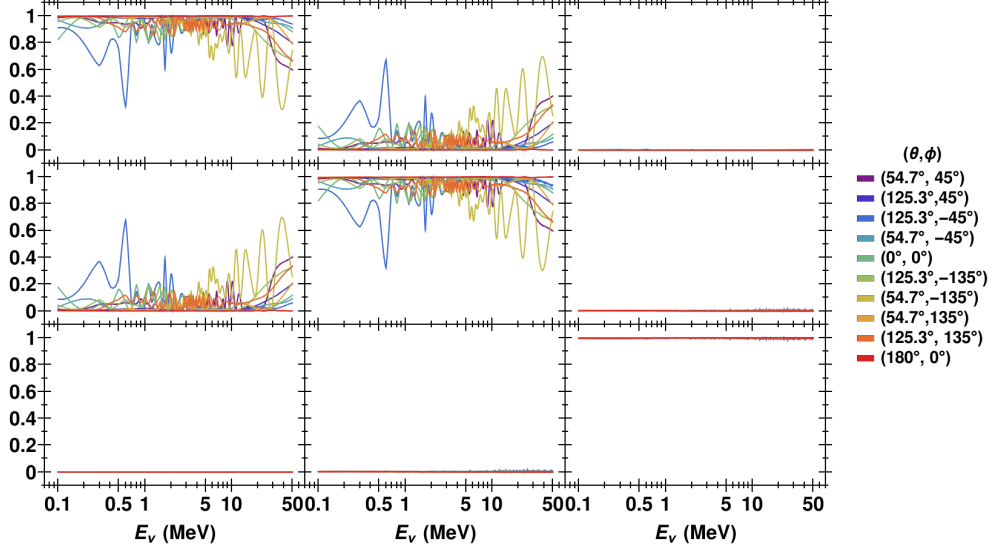
FIG. 11. The neutrino matter basis transition probabilities for inverted mass ordering at $t = 2.9$ **s**. The structure and layout is the same as that of Fig. 5.
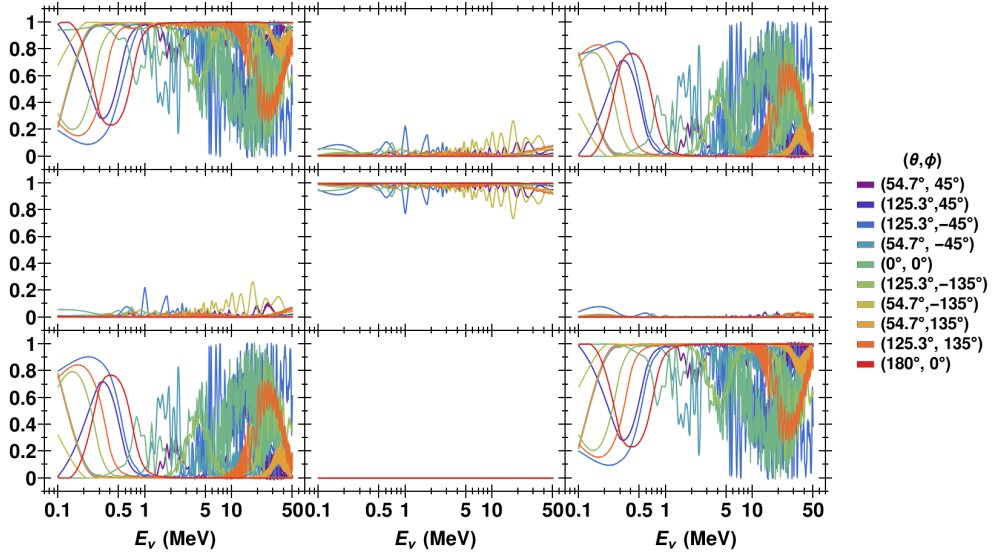

FIG. 12. The antineutrino matter basis transition probabilities for inverted mass ordering at $t = 2.9$ **s**. The structure and layout is the same as that of Fig. 5.

to an IMO. Now we observe the mixing involving ν_3 remains adiabatic at all energies while the mixing between ν_1 and ν_2 at $E \lesssim 5$ MeV is less adiabatic but for $E \gtrsim 5$ MeV it is more adiabatic. In the antineutrinos $\bar{P}_{22}^{(m)}$ is much less affected by the turbulent deflagration ash than $\bar{P}_{11}^{(m)}$ and $\bar{P}_{33}^{(m)}$ which are now the channels where strong variability of the transition probabilities is found.

An analysis of the causes of the large amplitude variability in the matter transition probabilities

during the detonation neutrino burst seen in Figs. 9 to 12 at $t = 2.9$ s indicates they are due to the aforementioned density discontinuities present in the deflagration ash layer on the 'surface' of the star. The neutrinos emitted during the detonation burst are produced in regions which lie interior to the ash and thus must pass through these density discontinuities as they exit the supernova. The densities in the deflagration ash layer located on the surface are similar to the resonance densities of the high (H) and low (L) Mikheyev-Smirnov-Wolfenstein (MSW) resonances [40] for the neutrino energies we consider. This setup is a recipe for the emergence of strong phase effects in the matter transition probabilities - compare with the results from Lund & Kneller [41] for the case of core-collapse neutrinos. The phase effects appears to be greatest in the H resonance channels - $\nu_2 \leftrightarrow \nu_3$ for a NMO, $\bar{\nu}_1 \leftrightarrow \bar{\nu}_3$ for a IMO. A more detailed discussion of the oscillation phenomenology, including turbulent and phase effects, can be found in Paper I [24].

B. Flavor basis transition probabilities at Earth

Once the matter basis oscillation probabilities are calculated we need to account for decoherence and then perform a basis change in order to compute the flavor basis transition probabilities at Earth. The details of this process are, again, given in Paper I and so here we will again just discuss some of the results. Figures 13 and 15 show $P_{ee}(E_\nu)$ on Earth for both NMO and IMO respectively. The different black lines in these figures represent the ten neutrino trajectories considered and each subplot is for a different time slice. In a similar fashion, but for antineutrinos, Figs. 14 and 16 show $\bar{P}_{ee}(E_\nu)$ on Earth for both NMO and IMO respectively. These figures reveal that much of the oscillation phenomenology discussed in the Sec. IV A for the matter basis at the edge of the supernova is also seen in the flavor basis at Earth. Namely: 1) At all epochs the effect of diabatic propagation is to increase the electron flavor survival probability from $\sim 0\%$ in the NMO and $\sim 30\%$ in the IMO. The electron antineutrino survival probability only decreases in the NMO from $\sim 70\%$ due to diabaticity but increases from $\sim 0\%$ in the IMO. 2) At early times ($t \lesssim 0.6$ s), the line-of-sight dependence is present only for energies above a threshold (which varies between 1 and 5 MeV) and it is largely binary (all lines of sight can be grouped into those that traverse the deflagration plume and those that do not). For these early times, it is also clear the evolution of the survival probabilities appears to be smoothly energy dependent. This stands in contrast to the more chaotic variations seen at later times. 3) At later times ($t \gtrsim 0.6$ s) and for neutrinos and NMO (Fig. 13) or for antineutrinos and IMO (Fig. 16), the highly discontinuous density profile of the SN imprints itself upon the survival probabilities leading to variations of up to 40%
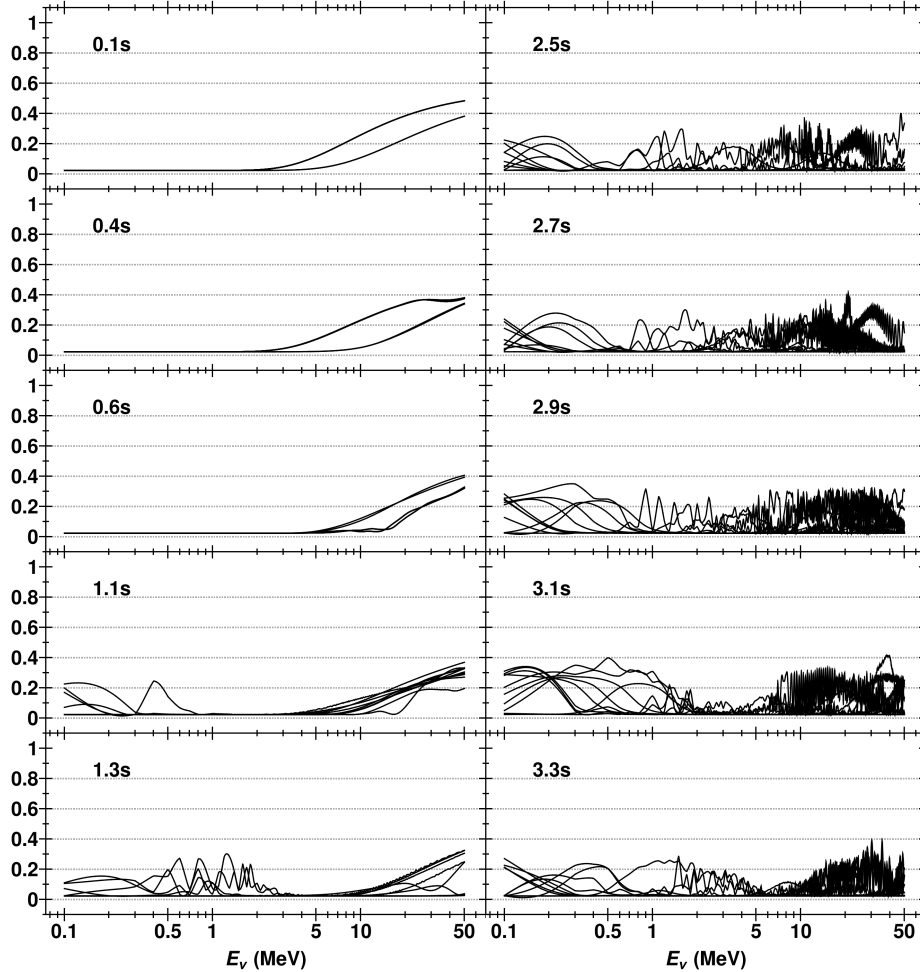
FIG. 13. The electron neutrino survival probability P_{ee} at Earth as a function of neutrino energy for each of the ten lines-of-sight through the simulation at the ten snapshot times. The mass ordering is normal.

for neutrinos in the NMO and 70% for antineutrino in the IMO. This variability occurs across the whole range of energies considered and persists for the full duration of the neutrino signal after $t > 0.6$ s. 4) For late times ($t \gtrsim 0.6$ s) the turbulence and phase effects in the neutrinos if the mass ordering is inverted (Fig. 15) or in the antineutrinos if the ordering is normal (Fig. 14) are much smaller in scale.

C.   The neutrino flux at Earth

In order to calculate the flux seen by a detector, we combine the neutrino transformation probabilities at Earth (Sec. IV B) with the luminosity (Sec. III) and then divide by a distance-dependent area factor. The distance used is $d = 10$ kpc, the commonly-used standard for Galactic supernovae and close to the most probable distance to a SN Ia of 9 kpc computed by Adams et
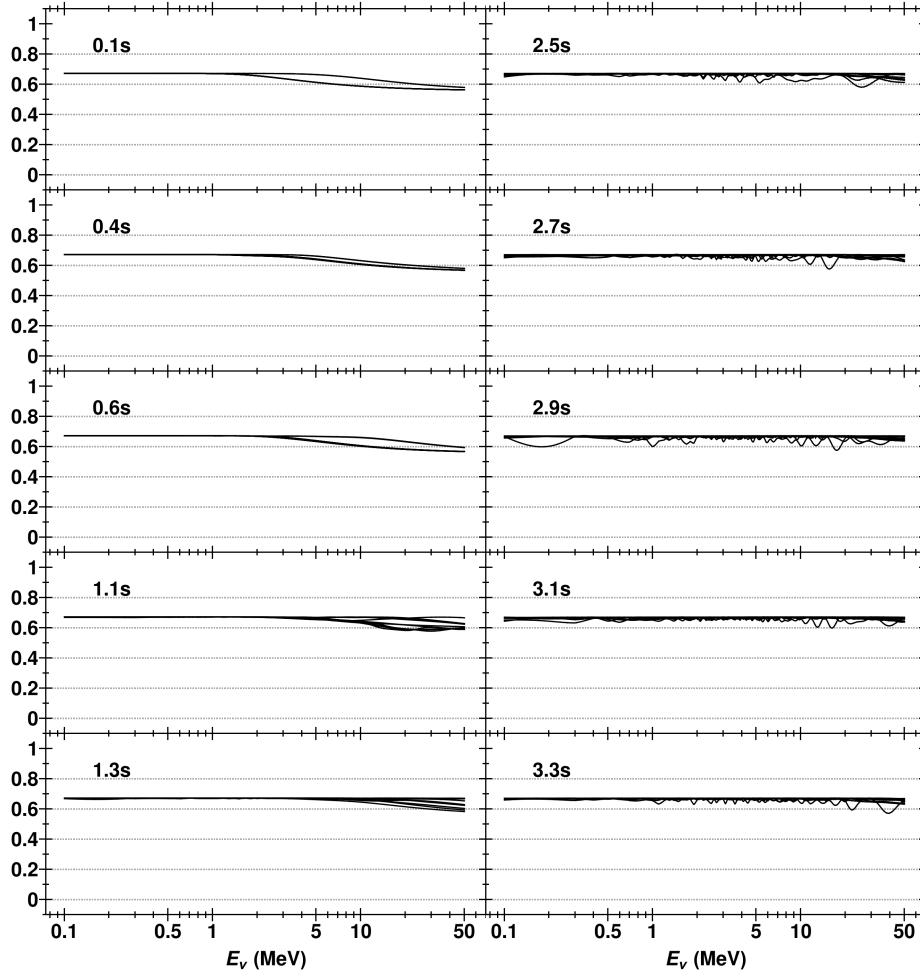
FIG. 14. The electron antineutrino survival probability $\bar{P}_{ee}$ at Earth as a function of neutrino energy for each of the ten lines-of-sight through the simulation at the ten snapshot times. The mass ordering is normal.

al. [17]. These fluxes at Earth are presented in Figs. 17 and 18 while the unoscillated neutrino flux at Earth is shown in Fig. 19 for comparison. In each case the flux has been split into the two neutrino bursts; the deflagration burst is represented by the top six panels and the detonation burst is represented by the bottom six panels. For the oscillated figures, all ten of the angular neutrino trajectories considered are plotted and the space between the highest and lowest at a given energy is shaded in order to indicate the variation due to line-of-sight dependence.

For the deflagration neutrino burst (top plots of Figs. 17 to 19) it is clear to see that the dominant ν_e flux has been largely oscillated into ν_μ and ν_τ. The same is true for the detonation burst (bottom plots of Figs. 17 to 19) though the effect is less severe because the ν_e flux is less dominant over the emitted ν_μ and ν_τ flux in the detonation burst epoch. In all cases the 10 MeV production feature in the ν_e spectrum is seen in the ν_μ and ν_τ spectra due to the effect
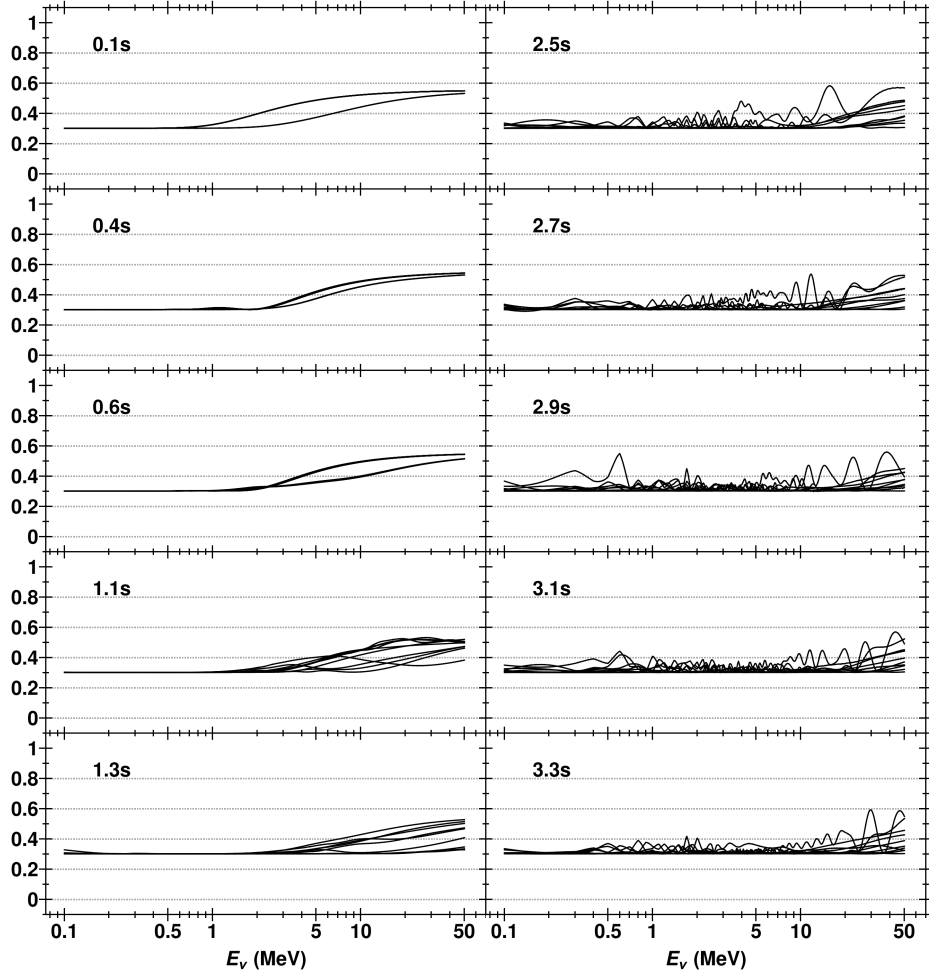
FIG. 15. The same as figure (13) but for an inverted mass hierarchy.

of the neutrino oscillations. It is worth pointing out that the 10 MeV feature is present in both the deflagration and the detonation burst. However, in the deflagration burst the 10 MeV peak develops midway through the burst. In contrast, for the detonation burst, the 10 MeV peak exists for the whole burst. Line-of-sight variation of the flux is almost an order of magnitude at some energies and the variation is most pronounced in the neutrino flux for NMO and in the antineutrino flux for IMO.

V. NEUTRINO DETECTION

Finally, with the neutrino fluxes at Earth in hand, we can process them through a range of neutrino detectors and compute the expected event rates for the GCD SN Ia in order to determine the detectability of the various production and oscillation features uncovered in the previous sec-

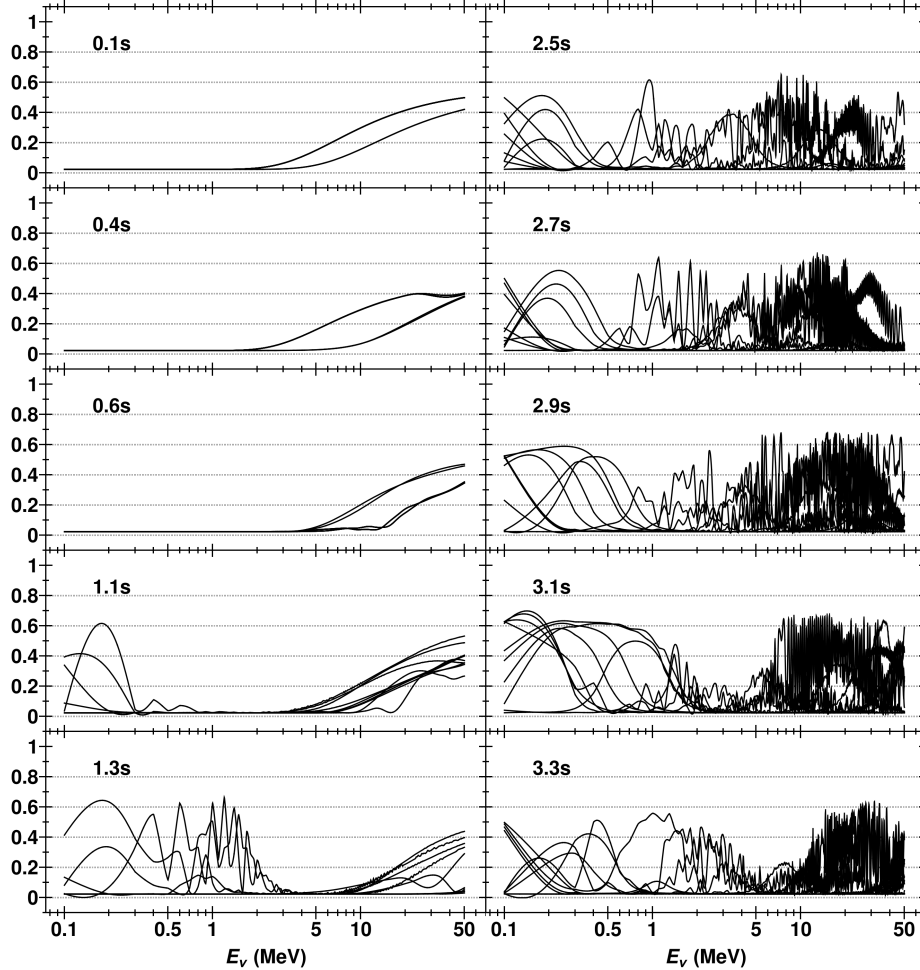

FIG. 16. The same as figure (14) but for an inverted mass hierarchy.

tions. The detectors under consideration are listed in Table II and are chosen because they are representative of various current and near-future neutrino detector technologies. The event rates in Super-K, Hyper-K[1], DUNE, and JUNO were calculated using SNOwGLoBES [42] and the event rate for IceCube was calculated according to the method described in Paper I. With the exception of Fig. 23, all of the results presented represent event counts where perfect detector efficiency is assumed and where energy smearing between the incoming neutrino and the detected lepton is ignored. The detectors in Table II are named with the suffix "like" to indicate that the configuration used only approximates the actual (or planned) detector. This is because, for the existing detectors, accurate configurations are not publicly available, and for future detectors, configuration information is not yet finalized. Although SNOwGLoBES gives results for each interaction channel

---

[1] We are aware that the planned configuration of Hyper-K has changed. The old configuration is used here because the details of the new configuration are not yet available and for consistency with Paper I. To first order, the results presented here can be scaled by detector mass.
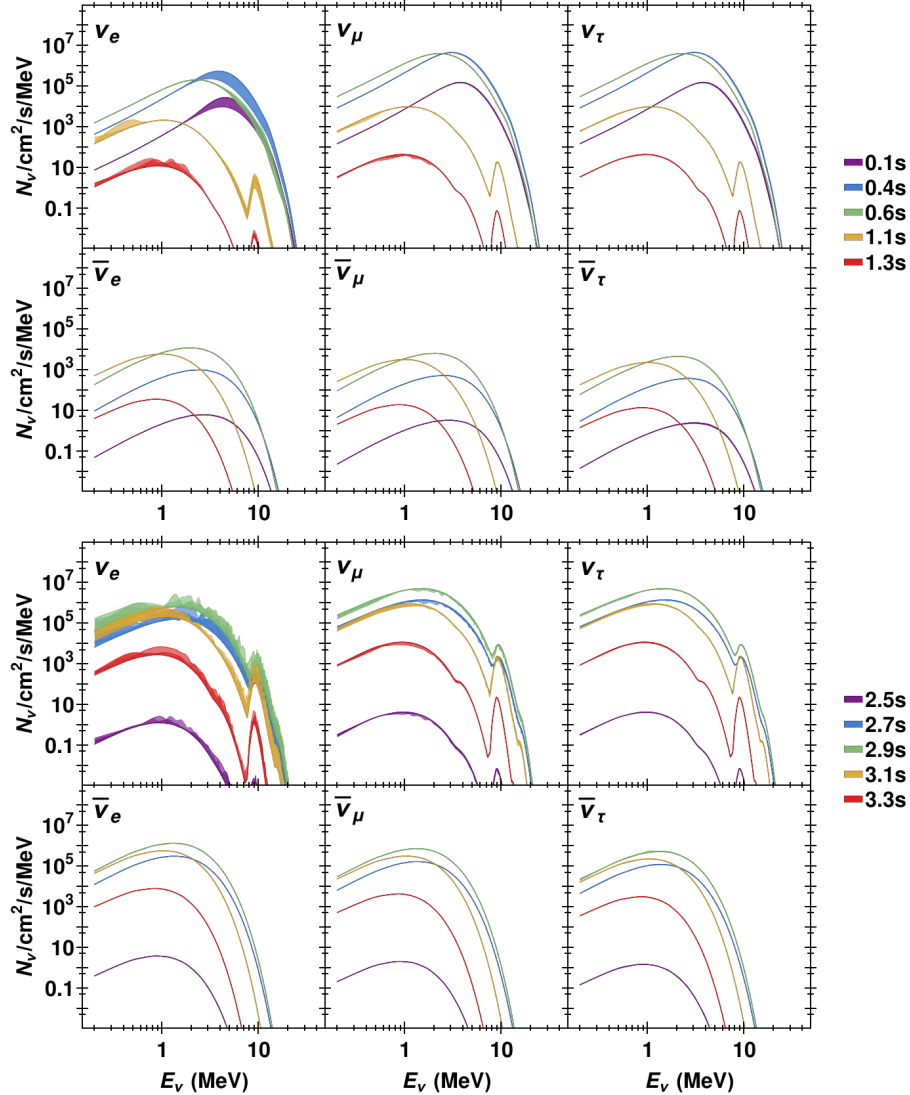
FIG. 17. The neutrino and antineutrino flux for each flavor from the GCD simulation at 10 kpc after oscillations for a NMO. Line thickness represents line-of-sight variation. In the top figure are the five snapshot times during the deflagration phase $t = 0.1$ s to $t = 1.3$ s, the bottom figure shows the flux during the detonation phase $t = 2.5$ s to $t = 3.3$ s. The color of each line indicates the snapshot time shown in the legend to the right of the figures.

separately, all the results we present are for the sum over all interaction channels.

Table III displays the number of interaction events in the detectors under consideration from a GCD SN Ia at 10 kpc. In addition to all channels, these numbers are for all energy bins and integrated over the full duration of both neutrino bursts. Furthermore, the displayed event counts are the mean over all 10 lines of sight considered. The line-of-sight variation is $\sim 5\%$ in NMO and $\sim 2\%$ in IMO. The lack of significant line-of-sight dependence means there is little ambiguity
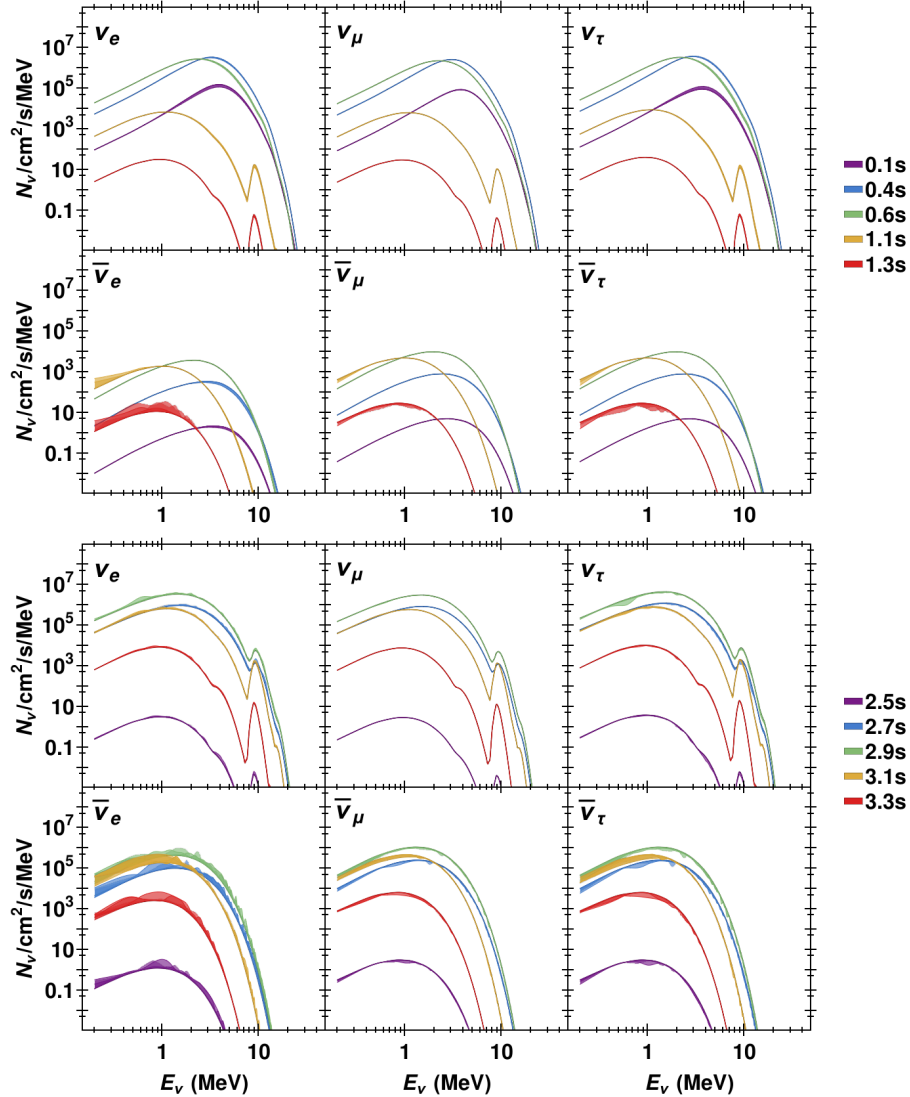
FIG. 18. The same as figure (17) but for an IMO.

Detector	Type	Mass (kt)
Super-Kamiokande like: 30% phototube coverage	Water Cherenkov	50
Hyper-Kamiokande like	Water Cherenkov	560
DUNE like detector	Liquid Ar	40
JUNO like detector	Scintillator	20
IceCube	Water Cherenkov	3500*

TABLE II. Summary of the detectors under consideration. Note that event rates simply scale by mass. *For IceCube, the mass given is the effective mass used for the event rate calculation (see Appendix A of Paper I [24]).

and uncertainty in the interpretation of our results. It is remarkable that the total signal has such a small line-of-sight variation considering how asymmetric the GCD simulation is. This is
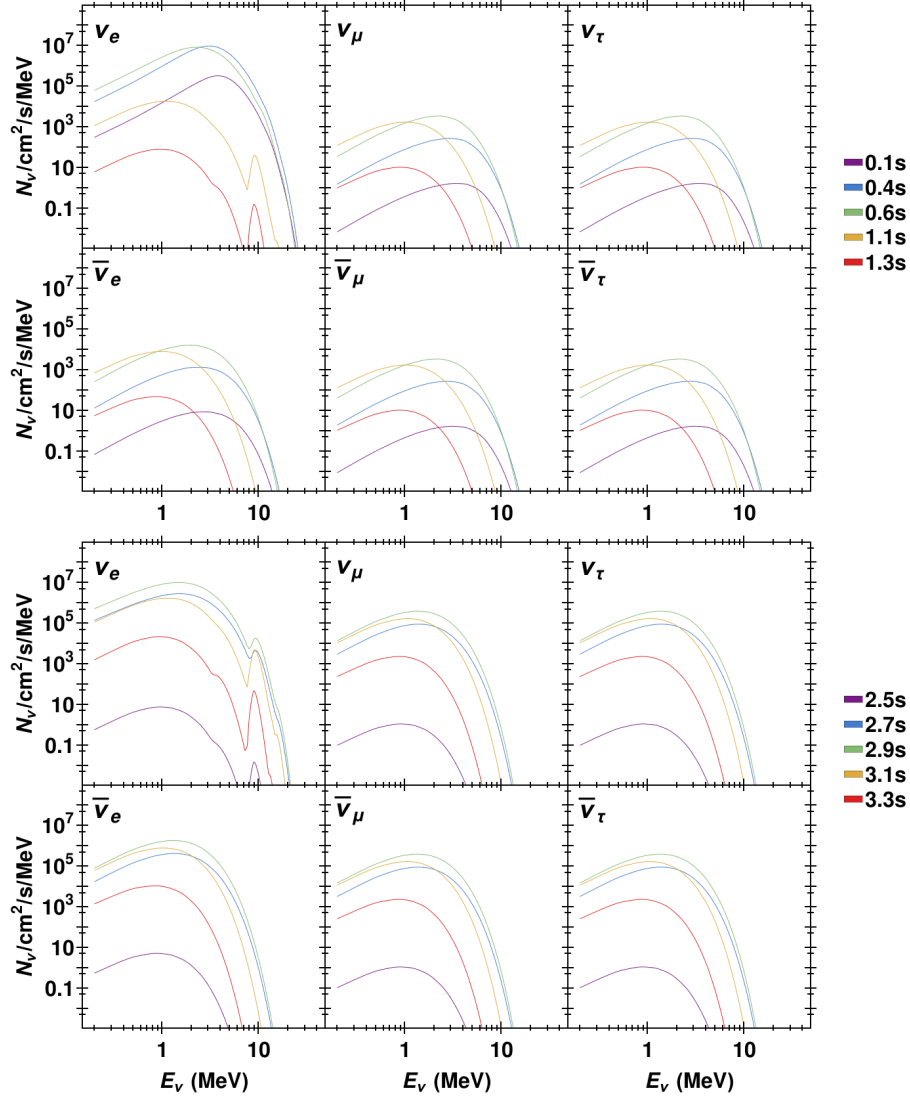
FIG. 19. The neutrino and antineutrino flux for each flavor from the GCD simulation at 10 kpc in the absence of flavor oscillations. In the top figure are the five snapshot times during the deflagration phase $t = 0.1$ s to $t = 1.3$ s, the bottom figure shows the flux during the detonation phase $t = 2.5$ s to $t = 3.3$ s. The color of each line indicates the snapshot time shown in the legend to the right of the figures.

a consequence of a lower line-of-sight variation during the time periods and at the energies of maximum neutrino emission. The table also shows the event rates in the same five detectors when we switch off neutrino flavor oscillations. Accounting for different detector masses and assumed distances, the number of events listed in this column are about a factor of 2-3 smaller than the number of events listed in Table 2 of Odrzywolek & Plewa for their Y12 model for comparable detectors.

The results in Table III demonstrate the well-known fact that neutrino flavor transformation

Detector	NMO	IMO	Unoscillated
Super-Kamiokande	0.0024	0.0043	0.0089
Hyper-Kamiokande	0.0267	0.0478	0.0997
DUNE	0.0015	0.0033	0.0069
JUNO	0.0010	0.0018	0.0037
IceCube*	0.0208	0.0325	0.0689

TABLE III. Numbers of interactions per detector for each mass ordering and a SN at 10 kpc. These event counts are for the whole 3.3 s neutrino burst averaged over the ten lines-of-sight considered. The fourth column represents the number of interactions observed when neutrino oscillations are not taken into account. * Note that the numbers of interactions quoted for IceCube are after background subtraction.

generally reduce the signal expected from SNe Ia without oscillations. For an IMO there are roughly only half as many events; for an NMO the number of events is reduced by a factor ~ 4. The overall reduction due to oscillation is caused by transformation of the flavor which dominates the emission at the source, ν_e, into other flavors at Earth. If the neutrinos propagated adiabatically then the electron neutrinos at the source would all but disappear into ν_μ and ν_τ for a NMO, and for an IMO we would observe only 30% of the original ν_e. Even though we find the neutrinos do not propagate adibatically at all energies and for all epochs, the diabaticity introduced by both the steep density gradients at the edge of the star and the multiple discontinuities in the deflagration ash is unable to increase the event rates by factors greater than a few.

Clearly a GCD SN Ia at 10 kpc will not be visible in any of the detectors listed in the table. If we change the distance to the supernovae the event rates scale as $(10 \text{ kpc}/d)^2$. Thus it would require the distance to the supernova be reduced to 1 kpc before Hyper-K and IceCube would only see a few interaction events. It is important to note that while the predicted number of interaction events in IceCube is similar to the number predicted in Hyper-K, the background separation is more demanding in IceCube. Hence, detection in IceCube would optimistically require a SN within ~ 50 pc to be seen as a greater than 1σ deviation above the background. For Super-K, JUNO, and DUNE we would need a GCD SN Ia at ~ 0.3 kpc to see a few interaction events. According to Adams et al. [17], the probability of a SN Ia being within 1 kpc is only $\sim 0.2\%$.

In addition to distance, we should not forget the event rate in a detector also scales by the detector mass (ignoring changes in detection efficiency). From the results in the table we see that one would need approximately a 10 Mt water Cherenkov detector to detect a galactic GCD SN Ia at the most probable distance of 10 kpc. This is similar to the 5 Mt detector considered by Kistler *et al.* [43].

Even though the neutrino detection probability of a galactic GCD SN Ia is quite low, if the
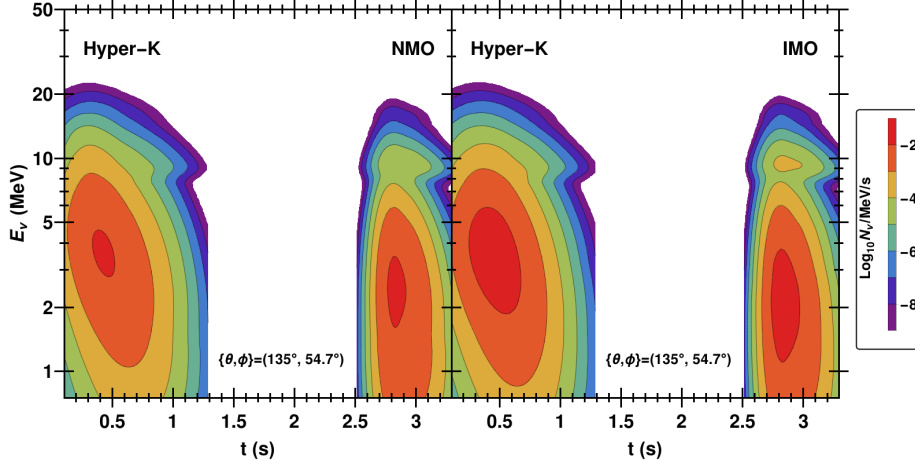
FIG. 20. A plot of the interaction event rate in Hyper-K for a particular line of sight for a GCD SN Ia at 10 kpc. The left column is for NMO and the right column is for IMO.

supernova is close and next-generation neutrino detectors are sufficiently large, it would be possible to go beyond total event rates and try to determine whether features in the signal can be discerned by examining the time and energy structure of the neutrino signal. Figure 20 show the differential interaction event rate in Hyper-K as a function of time and energy. Both mass orderings are displayed and one particular line of sight was chosen (neither the line of sight along the ignition points of the deflagration nor detonation). This figure demonstrates a clear distinction between the deflagration burst (0.1 s $< t < 1.3$ s) and the detonation burst (2.5 s $< t < 3.3$ s). The peak energy during the deflagration burst is ~ 4 MeV and ~ 2 MeV during the detonation burst. The 10 MeV production peak is mostly washed out during the deflagration peak but is clearly visible for the detonation peak. Lastly, the line-of-sight variation to Fig. 20 is small and does not change the above observations. Similar figures for the other detectors we are considering show similar structure.

We integrate the differential interaction event rates over energy and produce Fig. 21 which shows the differential interaction event rate from a GCD SN Ia at 10 kpc for Hyper-K, Super-K, DUNE, and JUNO. The line-of-sight variation is represented by the curve thickness, both mass orderings are shown, and the horizontal dotted lines indicate how the rate would shift for SNe at closer distances. This figure reveals that the line-of-sight variation is most prominent for $t < 0.5$ s. At these early times, the line-of-sight variation is because the deflagration plume is very asymmetric and thus lines of sight that traverse the plume will result in markedly different signals compared to those lines of sight that do not traverse the deflagration plume. Once the deflagration engulfs the star, the variation decreases due to the overall increase in adiabaticity. Another interesting
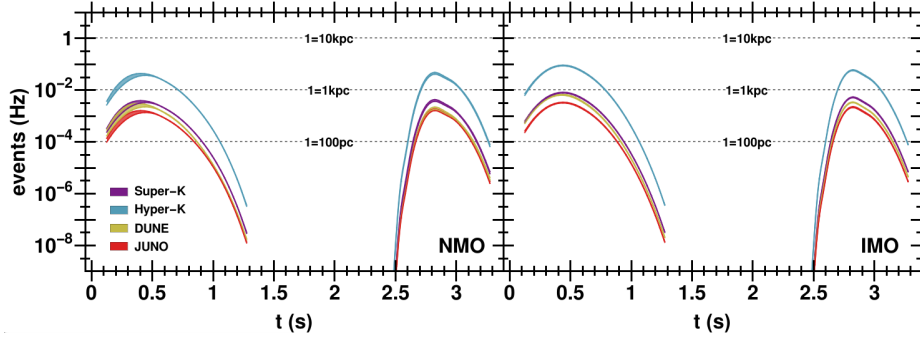
FIG. 21. The energy-integrated interaction event rate in Hyper-K, Super-K, DUNE, and JUNO for a GCD SN Ia at 10 kpc. The curve thickness indicates line-of-sight variation and the horizontal lines show how the rate (y-axis) would shift for nearer SN. The left column is for NMO and the right column is for IMO.

feature is that the detonation burst produces roughly as many events as the deflagration burst making this explosion-mechanism-differentiating feature just as visible as the signal as a whole. We also see the distinct separation of the deflagration and detonation bursts in the GCD scenario, with an estimated ~1.2 s gap between the bursts. As pointed out by Odrzywolek & Plewa [21], this double-peak time structure of the signal has great potential to distinguish the GCD explosion mechanism from other explosion mechanisms if the supernova occurs in sufficient proximity.

Finally, we can integrate the differential interaction event rates over time and look at spectral features. The results are shown Fig. 22 and, as before, curve thickness represents line-of-sight variation, both mass orderings are displayed, and both bursts, as well as the spectrum obtained by combining them. As observed from Fig. 20, we see the peak energy for the deflagration burst is greater than that of the detonation burst. The line-of-sight variation is mostly confined to energies greater than 4 MeV for the deflagration burst. In contrast the line-of-sight variation in the detonation burst is visible across the whole spectrum. Line-of-sight variation is also larger for NMO than for IMO. Of particular note is the 10 MeV spectral bump discussed in Sec. III which we find is only distinguishable in the detonation peak. However the figure indicates Super-K, JUNO, and DUNE would need a SN within 10 pc to detect the 10 MeV feature while Hyper-K would be able to distinguish the 10 MeV peak at ~ 30 pc. A supernova this near is quite unlikely.

Thus far we have only reported interaction events where the detected energy is that of the incoming neutrino. A more realistic approach is to examine the events as a function of the energy of the detected final state interaction products, smeared according to detector resolution. SNOwGLoBES provides event rates smeared according to distribution of final state products observed in a given detector. Figure 23 displays how the results shown in Fig. 22 will change with energy smearing
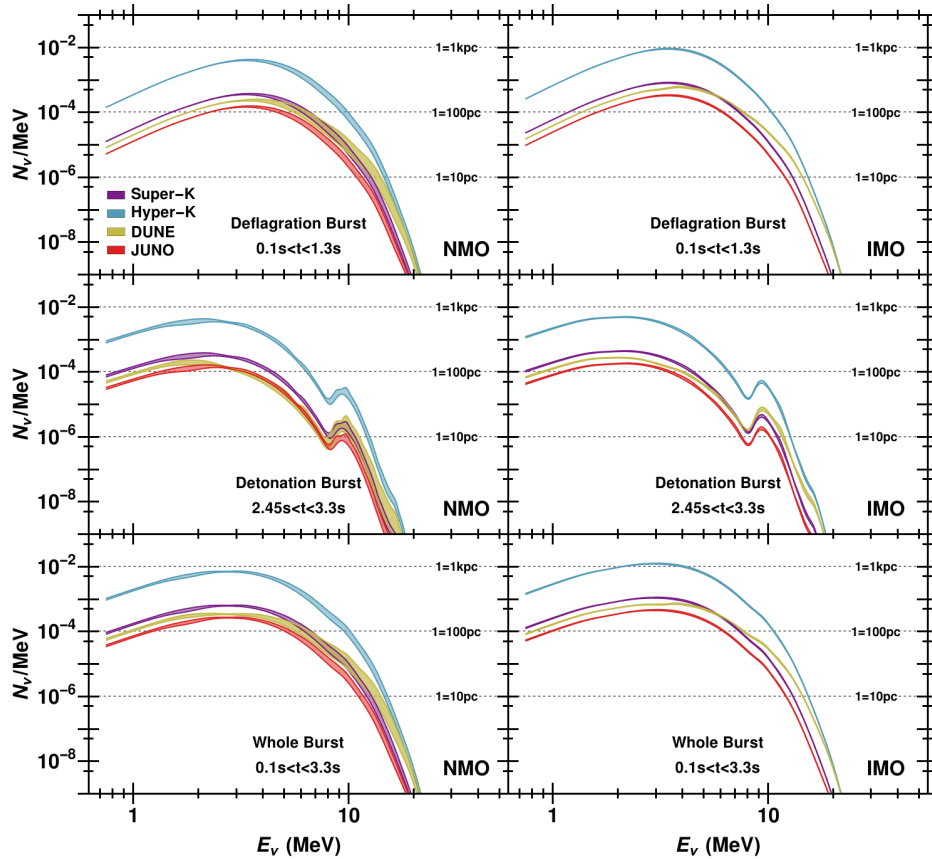
FIG. 22. The detector event spectrum in Hyper-K, Super-K, JUNO, and DUNE for a GCD SN Ia at 10 kpc. The curve thickness and shading indicates line-of-sight variation and the horizontal lines show how the rate (y-axis) would shift for nearer SN. The top row are for deflagration burst (0.1 s < t < 1.3 s), the middle row for the detonation burst (2.5 s < t < 3.3 s), and the bottom row are for the whole neutrino signal (0.1 s < t < 3.3 s). The left column is for NMO and the right column is for IMO.

taken into account. Only Hyper-K and DUNE are considered and the unsmeared interaction event energy is displayed as a gray background. The x-axis now represents the detected energy. The 'peak' seen in the Hyper-K spectrum is not a displaced 10 MeV peak; rather it is a consequence of the approximate smearing function. However, the 10 MeV peak seen in the DUNE spectrum is the 10 MeV production feature that has been displaced to approximately 8 MeV because of the smearing. Therefore, our approximate smearing techniques show that energy smearing drastically reduces the visibility of the 10 MeV peak in Hyper-K but only shifts it for DUNE.
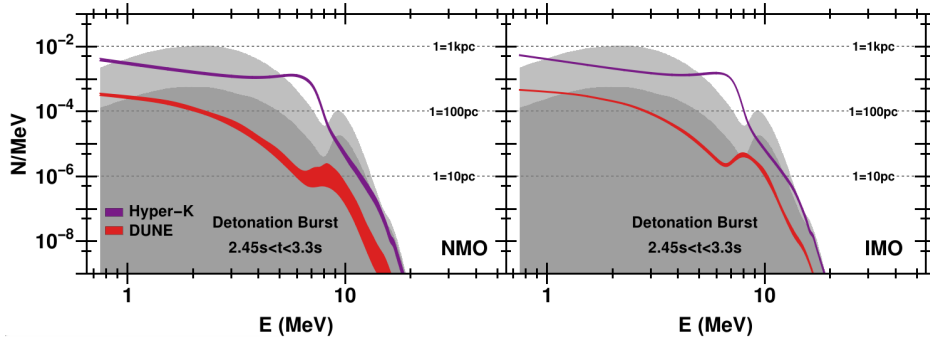
FIG. 23. The detector event spectrum in Hyper-K and DUNE for a GCD SN Ia at 10 kpc integrated over the detonation burst i.e for 2.5 s $< t <$ 3.3 s. The left column is for NMO and the right column is for IMO. The thickness of the red and purple curves indicate the line-of-sight variation and the horizontal lines show how the rate (y-axis) would shift for nearer SN. Detector energy smearing has been applied to the red and purple curves. The background gray curves represent the un-smeared event counts for comparison: the dark gray is for DUNE, the lighter gray for Hyper-K.

VI. GCD VERSUS DDT

In this last section we turn our attention to comparing the neutrino signal from the DDT SN Ia considered in Paper I to the GCD SN Ia neutrino signal described above. The neutrino emission from both the DDT and GCD is comprised of an early burst from a period of deflagration burning which transitions to a second burst of neutrino emission from a detonation phase. The big difference between the two scenarios is the ratio of neutrino luminosity from the two phases and the time between them. This difference is shown in Table IV where we list the peak neutrino luminosity as calculated for the two explosion mechanisms during the two phases and the times at which they occur. Firstly, the table shows the DDT model has more than an order of magnitude more luminosity when compared to the GCD model. This is reflected in both the maximum luminosity and the integrated luminosity. However we notice the peak luminosity during the detonation is much greater for the GCD model than for the DDT model. This means that, even though the DDT model emits more neutrinos, it is the GCD model that has the strongest detonation peak. Secondly, the time separation between the deflagration and the detonation burst is much larger for the GCD model than for the DDT model. After the overall event count difference, this time separation feature, if it can be detected, is a clear discriminating difference between the two models.

The features mentioned above are also clear from Fig. 24 where the neutrino luminosity is plotted against time. In this figure, the emission arising from weak and pair annihilation processes

Model	Deflagration		Detonation		Total
	time	erg/s	time	erg/s	erg
DDT	0.53 s	5.1×10^{49}	1.32 s	2.3×10^{47}	2.0×10^{49}
GCD	0.45 s	2.3×10^{48}	2.82 s	1.8×10^{48}	1.2×10^{48}

TABLE IV. Comparison of the maximum luminosity between the DDT and the GCD SN Ia simulations. The maximum luminosity is given for both the deflagration and detonation bursts. Also given is the total integrated luminosity for each model. It is important to note that in-between the deflagration and the detonation bursts, the GCD has very little neutrino emission but the DDT still has emission $\sim 1.3 \times 10^{47}$ erg/s.
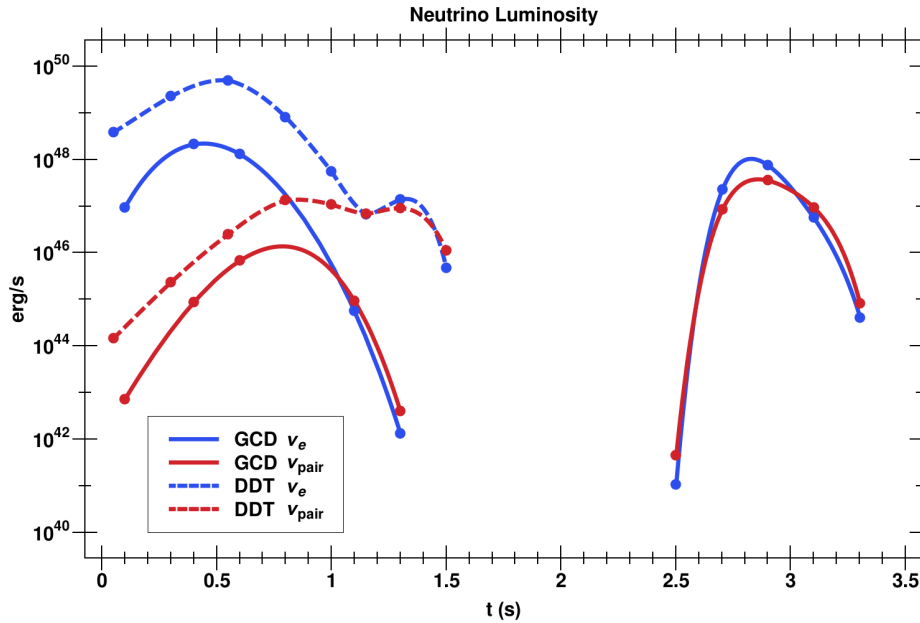

FIG. 24. A comparison of the neutrino luminosities for the DDT and GCD SN Ia simulations. The layout and structure is similar to that of Fig. 2

are shown separately. It is again clear that the DDT model has a greater luminosity than the GCD model and that the DDT model has a shorter gap between the deflagration and detonation bursts. Figure 24 shows another difference, namely that the DDT model still has significant neutrino emission in between the two bursts while the GCD model has practically no emission in between its deflagration and detonation bursts. An important feature that both the DDT and the GCD models share is that the deflagration burst is dominated by weak emission; however during the detonation burst, weak and thermal emission are equally important in both models.

But the neutrino emission is not the only way the two models differ. The degree to which neutrino oscillations affect the flux from both the DDT and the GCD models is shown Fig. 25. This figure only displays the differential spectrum of ν_e, ν_μ, and ν_τ at the peaks of the deflagration
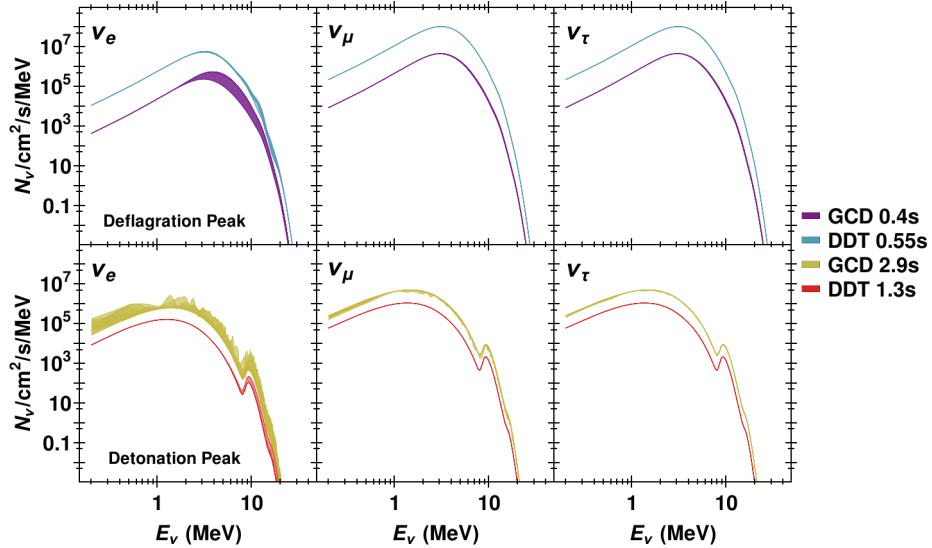
FIG. 25. A comparison of the differential neutrino flux on Earth for the DDT and GCD SN Ia simulations. The fluxes include the effects of oscillations for a NMO and $d = 10$ kpc. The three columns are for the three flavors of neutrinos. The top row shows the spectra at two snapshots during the deflagration burst of each simulation ($t_{\mathrm{GCD}} = 0.4$ s and $t_{\mathrm{DDT}} = 0.55$ s) and the bottom row shows the spectra at two snapshots during the detonation burst of each simulation ($t_{\mathrm{GCD}} = 2.9$ s and $t_{\mathrm{DDT}} = 1.3$ s). The simulation and the snapshot times are shown in the legend to the right. For each spectrum shown, the thickness of the curve indicates the range due to the line-of-sight variation through each calculation.

and detonation bursts for each of the models. The curve thickness denotes line-of-sight variation, the mass ordering is normal, and the distance to the SN is set to 10 kpc. It is clear that the DDT has the most flux during the deflagration phase and the GCD has the most flux during detonation. Also clear is the absence of the 10 MeV peak from the deflagration peak for both models, while the 10 MeV peak is present in the detonation peak of both models. The most important feature of Fig. 25 is found in comparing the line-of-sight variation of the two models. The DDT model has very little line-of-sight variation during the peak emission. Conversely, the GCD has much more line-of-sight variation during its peak emissions. This is not surprising when one considered how much more the GCD model departs from spherical symmetry when compared to the DDT model.

The differences between the two models in both the emitted spectra and flavor oscillations are preserved in the neutrino spectra at Earth and the event rates one expects in the various detectors we have considered. Figure 26 shows the event rate in Hyper-K and DUNE for both the DDT and the GCD models. Both mass orderings are presented, the error bars denote 3σ line-of-sight variation, the SN is at 10 kpc, and the horizontal lines indicate how the rates would change for nearer SN. This figure again indicates the line-of-sight variation is ten times greater in
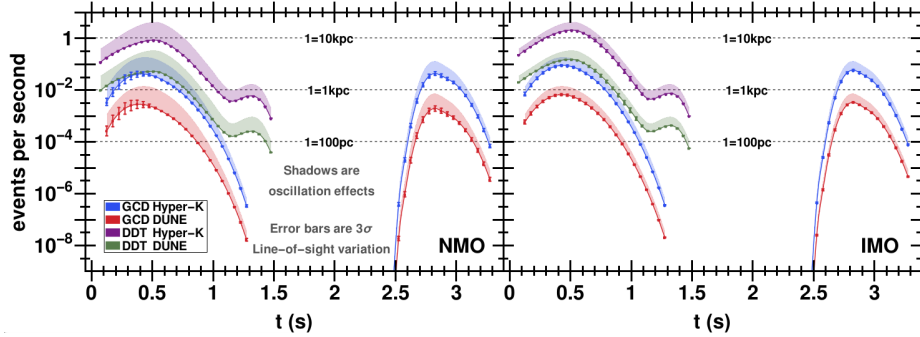
FIG. 26. The time evolution of the event rate in Hyper-K and DUNE for DDT and GCD simulations of a SN Ia at 10kpc. The shadowed regions represent the effects of neutrino oscillation such that the top of each shadowed region represents the associated un-oscillated event rate. The lines represent the mean event rate across all neutrino trajectories considered. Similarly, the error bars represent the 3σ deviation due to line-of-sight variations in the event rates. The left (right) plot is for normal (inverted) mass ordering. The horizontal lines show how the event rate would change if the supernova occurred at a closer distance.

GCD than DDT but still only a $<10\%$ correction. The line-of-sight variation in the GCD rates are most pronounced during $t < 0.5$ s while the DDT model has not appreciable variation at these times. Oscillation effects are roughly equally important in both models and the overall trend is that neutrino oscillations reduce the expected signal. The shaded area represents the effect of oscillations, i.e. the top of the shaded area corresponds to the rate if oscillations are ignored. It is striking that the main features observed from Table IV and Fig. 24 are clearly visible in Fig. 26. Namely, that the DDT has greater event rates and the GCD has a greater separation between bursts.

The overall event rate difference between the two models can be used to discriminate between them. In Fig. 27 we show the event counts in Hyper-K for the DDT and GCD models as a function of distance plus 1σ to 3σ uncertainty from Poisson noise and line-of-sight uncertainty. Assuming the distance to the supernova is known, the event rate alone can discriminate between the models at 2σ if the distance to the supernovae is less than $d \leq 2.26$ kpc for NMO and less than $d \leq 3.57$ kpc for IMO.

Similarly to Fig. 27, in Fig. 28 the overall event rate difference between the two neutrino mass orderings can be used to discriminate between them. In Fig. 28 we show the event counts in Hyper-K for the two neutrino mass hierarchies as a function of distance plus 1σ to 3σ uncertainty from Poisson noise and line-of-sight uncertainty. Assuming the distance to the supernova is known, the event rate alone can discriminate between NMO and IMO at 1σ if the distance to the supernovae
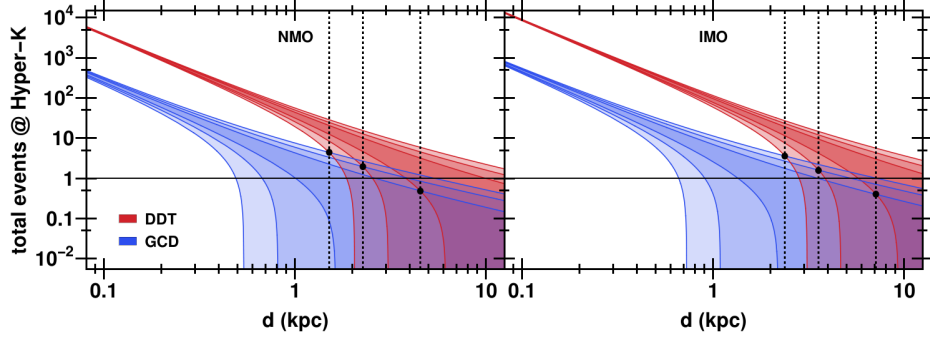
FIG. 27. The total number of events predicted to be measured in the Hyper-K detector as a function of the distance to the SN for both the DDT (red) and the GCD (blue) models. The left panel is for NMO and the right panel is the IMO. The shaded regions represent the event count range given a 1σ to 3σ Poisson error (also including a small error associated with line-of-sight uncertainty). The smallest, darkest shaded area represents the 1σ event range and the largest, lightest shaded area represents the 3σ event range for each model. The black dots show the distance at which the DDT total event count can be distinguished from the GCD total event count for a given σ confidence. For NMO these distances are, from left to right, $(d_{3\sigma}, d_{2\sigma}, d_{1\sigma}) = (1.51, 2.26, 4.52)$ kpc. For IMO these distances are, from left to right, $(d_{3\sigma}, d_{2\sigma}, d_{1\sigma}) = (2.38, 3.57, 7.13)$ kpc.
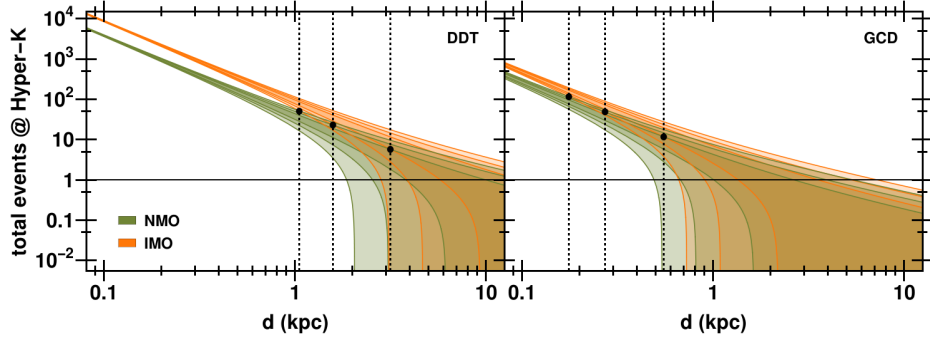

FIG. 28. The total number of events predicted to be measured in the Hyper-K detector as a function of the distance to the SN for both NMO (green) and IMO (orange). The left panel is for the DDT model and the right panel is the GCD model. The shaded regions represent the event count range given a 1σ to 3σ Poisson error (also including a small error associated with line-of-sight uncertainty). The smallest, darkest shaded area represents the 1σ event range and the largest, lightest shaded area represents the 3σ event range for each model. The black dots show the distance at which NMO can be distinguished from IMO for a given σ confidence. For DDT these distances are, from left to right, $(d_{3\sigma}, d_{2\sigma}, d_{1\sigma}) = (1.05, 1.58, 3.17)$ kpc. For GCD these distances are, from left to right, $(d_{3\sigma}, d_{2\sigma}, d_{1\sigma}) = (0.18, 0.27, 0.55)$ kpc.
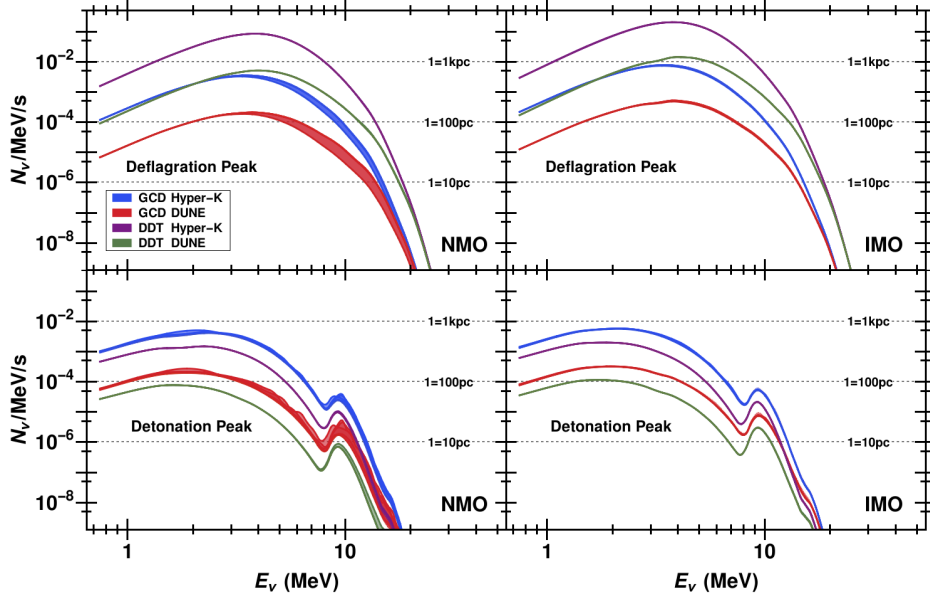
FIG. 29. The time evolution of the event rate spectra in Hyper-K and DUNE for DDT and GCD simulations of a SN Ia at 10kpc. The lines thickness represents the effect of line-of-sight variation. The left (right) plots are for normal (inverted) mass ordering. The horizontal lines show how the event rate would change if the supernova occurred at a closer distance. The top row represents the rate averaged over the deflagration burst and the bottom row represents the rate averaged over the detonation burst.

is less than $d \leq 3.17$ kpc for DDT and less than $d \leq 0.55$ kpc for GCD.

Lastly, Fig. 29 compares the event spectrum at both the deflagration and the detonation peaks for both models. This differential event rate shows the same features discussed in relation to Fig. 25. The new feature here is that we can quantify how much line-of-sight variation remains in the final interaction event rate spectrum. We see that even though there seems to be a significant amount of variation at higher energies, the variation near the peak of the emission is lower. Consequently, the line-of-sight variation for the GCD model is just a few percent and for the DDT model only a few tenth's of a percent when the total rate is considered. Thus, even though the GCD model has an order of magnitude more line-of-sight variation, the overall effect on the detected signal is small. Figure 29 shows that, apart from overall normalization, the neutrino spectra are very similar between the DDT and the GCD models. This is remarkable considering how very different the two explosions mechanisms are.

VII. CONCLUSION

In this paper we have studied neutrinos from a Gravitationally Confined Detonation scenario for a SN Ia in order to determine the features which might allow us to discriminate between this and other explosion mechanisms. Compared to earlier studies e.g. by Odrzywolek & Plewa [21], we have added a number of refinements to the calculation. We adopt a 3D SNe Ia simulation where previously 2D simulation was used, we calculate neutrino emission including more detailed spectral information, we include the effects of neutrino oscillations through the supernova by numerically solving the three-flavor evolution equations as a function of time, energy and for ten lines of sight, and we use a more complete detector modeling code SNOwGLoBES to compute the expected signal as a function of time and energy in a selection of detectors and for a variety of distances to the SN.

The results show that the GCD SN Ia produces two neutrino bursts. The first associated with deflagration burning with a peak luminosity of 2.3×10^{48} erg/s at $t = 0.45$ s. The second burst is associated with detonation burning with a peak luminosity of 1.2×10^{48} erg/s at $t = 2.82$ s. There is very little neutrino emission in between the two bursts. We also find a 10 MeV ν_e spectral feature associated with electron capture on copper appears at ~ 1 s during the deflagration burst which persists for the entirety of the detonation burst.

Neutrino oscillations introduce significant flavor conversion and are very line-of-sight dependent due to the discontinuity-ridden density profile and the asymmetrical explosion. The oscillations also deviate from adiabatic evolution across much of the time and energy parameter space. However, even though the oscillations show large line-of-sight dependence, the effect of line-of-sight variation on the total number of detected events is only a few percent.

The calculated interaction event rates show that, for a GCD SN Ia at 1 kpc, Hyper-K and IceCube would only see a few interaction events. While Super-K, JUNO, and DUNE would need a GCD SN Ia at $\sim$0.3 kpc to see a few interaction events. Thus the conclusion is that one would either need an improbably close SN or order-of-magnitude larger detectors than current and near future proposals to confidently observe the neutrinos from a SN Ia with a GCD explosion mechanism.

A comparison of the neutrino signals from the DDT SN and the GCD SN reveals several similarities features between them. The line-of-sight analysis shows that neither model would suffer from a great amount ($< 10\%$) of line-of-sight variation of the total detected events even though the GCD explosion is much more aspherical than the DDT. In both cases, inverted mass ordering yields more events than normal ordering but both are less then the case of no neutrino oscillations.

The 10 MeV neutrino spectral feature that is found in both DDT and GCD is difficult to detect even for next generation neutrino detectors because it appears at late times when the luminosity is low. However the comparison between the DDT and GCD also reveals two very important, explosion model distinguishing, features. Firstly, the DDT SN has an order of magnitude more overall neutrino emission than the GCD SN. If the distance to the supernova can be determined then the large difference in event rates - assuming events are detected - will allow discrimination between the two models. If the supernova is sufficiently close that a star which explodes as a GCD SN Ia produces events in a detector, the distinctive separation in time between the deflagration and detonation burst of this scenario will also allow discrimination between the two scenarios independent of the overall event rate diagnostic. And finally, SN Ia can also provide information about neutrino proerpties if the explosion mechanism and distance are known. We find, if the mechanism and distance are known, the overall event rate can be used to determine the neutrino mass ordering.

[1] M. M. Phillips, "The absolute magnitudes of Type IA supernovae," ApJ, vol. 413, pp. L105–L108, Aug. 1993.

[2] M. M. Phillips, P. Lira, N. B. Suntzeff, R. A. Schommer, M. Hamuy, and J. Maza, "The Reddening-Free Decline Rate Versus Luminosity Relationship for Type IA Supernovae," AJ, vol. 118, pp. 1766–1776, Oct. 1999.

[3] A. G. Riess, A. V. Filippenko, P. Challis, A. Clocchiatti, A. Diercks, P. M. Garnavich, R. L. Gilliland, C. J. Hogan, S. Jha, R. P. Kirshner, B. Leibundgut, M. M. Phillips, D. Reiss, B. P. Schmidt, R. A. Schommer, R. C. Smith, J. Spyromilio, C. Stubbs, N. B. Suntzeff, and J. Tonry, "Observational Evidence from Supernovae for an Accelerating Universe and a Cosmological Constant," ApJ, vol. 116, pp. 1009–1038, Sep. 1998.

[4] B. P. Schmidt, N. B. Suntzeff, M. M. Phillips, R. A. Schommer, A. Clocchiatti, R. P. Kirshner, P. Garnavich, P. Challis, B. Leibundgut, J. Spyromilio, A. G. Riess, A. V. Filippenko, M. Hamuy, R. C. Smith, C. Hogan, C. Stubbs, A. Diercks, D. Reiss, R. Gilliland, J. Tonry, J. Maza, A. Dressler, J. Walsh, and R. Ciardullo, "The High-Z Supernova Search: Measuring Cosmic Deceleration and Global Curvature of the Universe Using Type IA Supernovae," ApJ, vol. 507, pp. 46–63, Nov. 1998.

[5] S. Perlmutter, G. Aldering, G. Goldhaber, R. A. Knop, P. Nugent, P. G. Castro, S. Deustua, S. Fabbro, A. Goobar, D. E. Groom, I. M. Hook, A. G. Kim, M. Y. Kim, J. C. Lee, N. J. Nunes, R. Pain, C. R. Pennypacker, R. Quimby, C. Lidman, R. S. Ellis, M. Irwin, R. G. McMahon, P. Ruiz-Lapuente, N. Walton, B. Schaefer, B. J. Boyle, A. V. Filippenko, T. Matheson, A. S. Fruchter, N. Panagia, H. J. M. Newberg, W. J. Couch, and T. S. C. Project, "Measurements of Ω and Λ from 42 High-Redshift Supernovae," ApJ, vol. 517, pp. 565–586, Jun. 1999.

[6] K. Nomoto, K. Iwamoto, N. Nakasato, F.-K. Thielemann, F. Brachwitz, T. Tsujimoto, Y. Kubo, and N. Kishimoto, "Nucleosynthesis in type Ia supernovae," *Nuclear Physics A*, vol. 621, pp. 467–476, Feb. 1997.

[7] C. Kobayashi and K. Nomoto, "The Role of Type Ia Supernovae in Chemical Evolution. I. Lifetime of Type Ia Supernovae and Metallicity Effect," ApJ, vol. 707, pp. 1466–1484, Dec. 2009.

[8] W. Li, J. S. Bloom, P. Podsiadlowski, A. A. Miller, S. B. Cenko, S. W. Jha, M. Sullivan, D. A. Howell, P. E. Nugent, N. R. Butler, E. O. Ofek, M. M. Kasliwal, J. W. Richards, A. Stockton, H.-Y. Shih, L. Bildsten, M. M. Shara, J. Bibby, A. V. Filippenko, M. Ganeshalingam, J. M. Silverman, S. R. Kulkarni, N. M. Law, D. Poznanski, R. M. Quimby, C. McCully, B. Patel, K. Maguire, and K. J. Shen, "Exclusion of a luminous red giant as a companion star to the progenitor of supernova SN 2011fe," Nature, vol. 480, pp. 348–350, Dec. 2011.

[9] P. L. Kelly, O. D. Fox, A. V. Filippenko, S. B. Cenko, L. Prato, G. Schaefer, K. J. Shen, W. Zheng, M. L. Graham, and B. E. Tucker, "Constraints on the Progenitor System of the Type Ia Supernova 2014J from Pre-explosion Hubble Space Telescope Imaging," ApJ, vol. 790, p. 3, Jul. 2014.

[10] M. T. B. Nielsen, M. Gilfanov, Á. Bogdán, T. E. Woods, and G. Nelemans, "Upper limits on the luminosity of the progenitor of Type Ia supernova SN 2014J," MNRAS, vol. 442, pp. 3400–3406, Aug. 2014.

[11] D. Maoz, F. Mannucci, and G. Nelemans, "Observational Clues to the Progenitors of Type Ia Supernovae," ARA&A, vol. 52, pp. 107–170, Aug. 2014.

[12] P. Ruiz-Lapuente, "New approaches to SNe Ia progenitors," New A Rev., vol. 62, pp. 15–31, Oct. 2014.

[13] A. M. Khokhlov, "Delayed detonation model for type IA supernovae," A&A, vol. 245, pp. 114–128, May 1991.

[14] T. Plewa, A. C. Calder, and D. Q. Lamb, "Type Ia Supernova Explosion: Gravitationally Confined Detonation," ApJ, vol. 612, pp. L37–L40, Sep. 2004.

[15] E. Bravo and D. García-Senz, "Beyond the Bubble Catastrophe of Type Ia Supernovae: Pulsating Reverse Detonation Models," ApJ, vol. 642, pp. L157–L160, May 2006.

[16] W. Hillebrandt, M. Kromer, F. K. Röpke, and A. J. Ruiter, "Towards an understanding of Type Ia supernovae from a synthesis of theory and observations," *Frontiers of Physics*, vol. 8, pp. 116–143, Apr. 2013.

[17] S. M. Adams, C. S. Kochanek, J. F. Beacom, M. R. Vagins, and K. Z. Stanek, "Observing the Next Galactic Supernova," ApJ, vol. 778, p. 164, Dec. 2013.

[18] D. Falta, R. Fisher, and G. Khanna, "Gravitational Wave Emission from the Single-Degenerate Channel of Type Ia Supernovae," *Physical Review Letters*, vol. 106, no. 20, p. 201103, May 2011.

[19] I. R. Seitenzahl, M. Herzog, A. J. Ruiter, K. Marquardt, S. T. Ohlmann, and F. K. Röpke, "Neutrino and gravitational wave signal of a delayed-detonation model of type Ia supernovae," Phys. Rev. D, vol. 92, no. 12, p. 124013, Dec. 2015.

[20] T. Kunugise and K. Iwamoto, "Neutrino Emission from Type Ia Supernovae," PASJ, vol. 59, pp. L57–L61, Dec. 2007.

[21] A. Odrzywolek and T. Plewa, "Probing thermonuclear supernova explosions with neutrinos," A&A, vol. 529, p. A156, May 2011.

[22] H. Duan, G. M. Fuller, J. Carlson, and Y.-Z. Qian, "Simulation of coherent non-linear neutrino flavor transformation in the supernova environment. i: Correlated neutrino trajectories," *Phys. Rev.*, vol. 74, p. 105014, 2006.

[23] H. Duan, G. M. Fuller, J. Carlson, and Y.-Z. Qian, "Coherent development of neutrino flavor in the supernova environment," *Phys. Rev. Lett.*, vol. 97, p. 241101, 2006.

[24] W. P. Wright, G. Nagaraj, J. P. Kneller, K. Scholberg, and I. R. Seitenzahl, "Neutrinos from Type Ia Supernovae I: The Deflagration-To-Detonation Transition Scenario," *ArXiv e-prints*, May 2016.

[25] I. R. Seitenzahl, C. A. Meakin, D. Q. Lamb, and J. W. Truran, "Initiation of the Detonation in the Gravitationally Confined Detonation Model of Type Ia Supernovae," ApJ, vol. 700, pp. 642–653, Jul. 2009.

[26] T. Plewa, A. C. Calder, and D. Q. Lamb, "Type Ia Supernova Explosion: Gravitationally Confined Detonation," ApJ, vol. 612, pp. L37–L40, Sep. 2004.

[27] I. R. Seitenzahl, M. Kromer, S. T. Ohlmann, F. Ciaraldi-Schoolmann, K. Marquardt, M. Fink, W. Hillebrandt, R. Pakmor, F. K. Röpke, A. J. Ruiter, S. A. Sim, and S. Taubenberger, "Three-dimensional simulations of gravitationally confined detonations compared to observations of SN 1991T," A&A, vol. 592, p. A57, Jul. 2016.

[28] I. R. Seitenzahl, F. Ciaraldi-Schoolmann, F. K. Röpke, M. Fink, W. Hillebrandt, M. Kromer, R. Pakmor, A. J. Ruiter, S. A. Sim, and S. Taubenberger, "Three-dimensional delayed-detonation models with nucleosynthesis for Type Ia supernovae," MNRAS, vol. 429, pp. 1156–1172, Feb. 2013.

[29] M. Reinecke, W. Hillebrandt, J. C. Niemeyer, R. Klein, and A. Gröbl, "A new model for deflagration fronts in reactive fluids," A&A, vol. 347, pp. 724–733, Jul. 1999.

[30] G. M. Fuller, W. A. Fowler, and M. J. Newman, "Stellar weak interaction rates for intermediate-mass nuclei. II - A = 21 to A = 60," ApJ, vol. 252, pp. 715–740, Jan. 1982.

[31] K. Langanke and G. Martínez-Pinedo, "Shell-model calculations of stellar weak interaction rates: II. Weak rates for nuclei in the mass range /A=45-65 in supernovae environments," *Nuclear Physics A*, vol. 673, pp. 481–508, Jun. 2000.

[32] K. Langanke, G. Martínez-Pinedo, J. M. Sampaio, D. J. Dean, W. R. Hix, O. E. Messer, A. Mezzacappa, M. Liebendörfer, H.-T. Janka, and M. Rampp, "Electron Capture Rates on Nuclei and Implications for Stellar Core Collapse," *Physical Review Letters*, vol. 90, no. 24, p. 241102, Jun. 2003.

[33] A. Burrows, S. Reddy, and T. A. Thompson, "Neutrino opacities in nuclear matter," *Nuclear Physics A*, vol. 777, pp. 356–394, Oct. 2006.

[34] T. Oda, M. Hino, K. Muto, M. Takahara, and K. Sato, "Rate Tables for the Weak Processes of sd-Shell Nuclei in Stellar Matter," *Atomic Data and Nuclear Data Tables*, vol. 56, pp. 231–403, Mar. 1994.

[35] A. W. Steiner, M. Hempel, and T. Fischer, "Core-collapse Supernova Equations of State Based on Neutron Star Observations," ApJ, vol. 774, p. 17, Sep. 2013.

[36] E. O'Connor and C. D. Ott, "A new open-source code for spherically symmetric stellar collapse to neutron stars and black holes," *Classical and Quantum Gravity*, vol. 27, no. 11, p. 114103, Jun. 2010.

[37] C. Sullivan, E. O'Connor, R. G. T. Zegers, T. Grubb, and S. M. Austin, "The Sensitivity of Core-collapse Supernovae to Nuclear Electron Capture," ApJ, vol. 816, p. 44, Jan. 2016.

[38] L. Wolfenstein, "Neutrino oscillations in matter," Phys. Rev. D, vol. 17, pp. 2369–2374, May 1978.

[39] S. P. Mikheyev and A. Y. Smirnov, "Resonance enhancement of oscillations in matter and solar neutrino spectroscopy," *Yad. Fiz.*, vol. 42, p. 1441, 1985, (*Sov. J. Nucl. Phys.* **42** 913).

[40] A. S. Dighe and A. Y. Smirnov, "Identifying the neutrino mass spectrum from a supernova neutrino burst," Phys. Rev. D, vol. 62, no. 3, p. 033007, Aug. 2000.

[41] T. Lund and J. P. Kneller, "Combining collective, MSW, and turbulence effects in supernova neutrino flavor evolution," Phys. Rev. D, vol. 88, no. 2, p. 023008, Jul. 2013.

[42] "Snowglobes," http://www.phy.duke.edu/~schol/snowglobes/, accessed: 2016-02-01.

[43] M. D. Kistler, H. Yüksel, S. Ando, J. F. Beacom, and Y. Suzuki, "Core-collapse astrophysics with a five-megaton neutrino detector," Phys. Rev. D, vol. 83, no. 12, p. 123008, Jun. 2011.